Prediction of the energetic particle redistribution by an improved critical gradient model and analysis of the transport threshold

Y. Zou, V. S. Chan, M. A. Van Zeeland, et al.

View Online   Export Citation   CrossMark

ARTICLES YOU MAY BE INTERESTED IN

Prediction of the energetic particle redistribution by an improved critical gradient model and analysis of the transport threshold

Y. Zou,[1] V. S. Chan,[2,3,a] M. A. Van Zeeland,[2] W. W. Heidbrink,[4] Y. Todo,[5,6] Wei Chen,[1] Y. Wang,[1] and J. Chen[7]

AFFILIATIONS

[1]Southwestern Institute of Physics, P.O. Box 432, Chengdu 610041, China
[2]General Atomics, P.O. Box 85608, San Diego, California 92186-5608, USA
[3]School of Nuclear Science and Technology, University of Science and Technology of China, Hefei 230026, China
[4]University of California Irvine, Irvine, California 92697, USA
[5]National Institute for Fusion Science, Toki, Gifu 509-5292, Japan
[6]Department of Fusion Science, SOKENDAI (The Graduate University for Advanced Studies), Toki, Gifu 509-5292, Japan
[7]Institute of Plasma Physics, Chinese Academy of Sciences, Hefei 230031, China

[a]Author to whom correspondence should be addressed: chanvs@ustc.edu.cn

ABSTRACT

Based on the theory of critical gradient model (CGM) and following the simulation method proposed by Waltz *et al.* [Nucl. Fusion **55**, 123012 (2015)], a combination of TGLFEP and EPtran code is employed to predict the energetic particle (EP) transport induced by Alfvén eigenmodes (AEs). To be consistent with the experiment, recent improvements to the simulation method include consideration of threshold evolution and orbit loss due to finite orbit width. The revised CGM is applied to simulate two DIII-D experimental discharges (#142111 and #153071). It well reproduces the experimental profiles with multiple unstable AEs and large-scale EP transport. Discharge #142111 had previously been simulated using a nonlinear MHD-kinetic code MEGA [Todo *et al.*, Nucl. Fusion **55**, 073020 (2015)] with a transport mechanism based on stochasticity induced by overlapping AE. By comparing the simulated EP profiles, we find that the AE transport threshold is approximated by both the MEGA nonlinear stability threshold and the proposed CGM threshold (error <5% for single n and <17% for multiple n simulation). Both of them are larger than the linear stability threshold of the most unstable AE mode by a quantity of the order of the flux needed to sustain EP transport by the background turbulence. We have also applied the improved CGM to simulate the α particle redistribution for a China Fusion Engineering Test Reactor steady state scenario. Because of the clear separation between the AE unstable region and the loss cone, only a moderate α particle loss of ∼9.6% is predicted.

Published under an exclusive license by AIP Publishing. https://doi.org/10.1063/5.0078098

I. INTRODUCTION

Energetic particle (EP) distribution prediction is a key issue for future fusion reactors, including the China Fusion Engineering Test Reactor (CFETR),[1,2] which aims to achieve a self-sustainable burning state. In the past studies of EP physics in burning plasmas, a classical slowing down distribution[3,4] was typically applied as a rough estimate of the EP distribution. Unfortunately, recent DIII-D experiments indicated that the diagnosed EP profile deviated far from the classical prediction, in particular in cases with multiple unstable Alfvén eigenmodes (AEs).[5,6] Analogous phenomena were similarly observed

in other experimental devices.[7–10] Theoretically, EP spatial gradient is a primary driver for destabilizing a variety of AEs, which conversely enhance EP transport itself. It causes particles to move outward to flatten the EP density profile, thus reducing the EP gradient and suppressing the AE instabilities. A single unstable AE can cause EP transport due to the breaking of adiabatic invariants by microturbulence scattering.[11] This led to the proposal of a critical gradient model (CGM) with the linear stability of the most unstable AE as a threshold.[12,13] Alternatively, multiple unstable AEs at different spatial locations could overlap to cause stochastic diffusion,[14] which occurs when the

amplitude of AE is sufficiently large. A single AE can also cause orbit overlap in phase space, again the amplitude of AE needs to be sufficiently large.[15] The EP gradient threshold for significant diffusion is phase-space dependent and is shown to be higher than that of a single unstable mode calculated by linear stability.[16] Both models predict an explosive growth of EP transport when their thresholds are exceeded, which will rapidly redistribute the EPs to their respective marginal levels with suppressed AE transport (defined as AE transport threshold in this paper). Therefore, the details of the AE-induced transport may not be as crucial as the quantitative determination of the threshold value for determining the redistributed EP profile. Our study has two objectives. One is to apply the improved CGM to benchmark the predicted EP redistribution profiles with two DIII-D experimental discharges (#142111 and #153071). The second is to compare the transport threshold of CGM with that from a published nonlinear MHD-kinetic simulation by MEGA[17] of discharge #142111 and investigate the similarities and differences between the two thresholds. Unstable AEs could also change the trajectories of EPs leading to enhanced orbit losses. Additionally, the EP loss cone is more significant in the outer part of the plasma, so, by pushing confined EPs farther out, AE-induced transport can indirectly increase the loss fraction. Thus, EP distribution and AE stability in realistic tokamak geometry form a complex feedback system. Quantitative prediction of EP losses will require a closed-loop iteration between EP dynamics and AE stability with an accurate magnetic equilibrium. For realistic comparisons with experiments and the MEGA simulation, it is important for our CGM simulation to include finite orbit losses as well.

To interpret the differences between classical slowing down distribution and experimental profiles, various numerical models, such as ORBIT,[18] MEGA,[19,20] and kick model,[21,22] were developed, moving simulation predictions closer to the experiment. However, the self-consistent simulation of EP transport mechanisms is a computationally intensive effort. Thus, a reduced physics model, critical gradient model (CGM), using a few basic assumptions to predict the EP redistribution efficiently and make it more suitable for integrated modeling of reactor scenarios. AEs are driven by the EP pressure gradient, which has a threshold for marginally stable AE. The existence of the threshold was confirmed by theory[23,24] and experiment.[25] Above the threshold, AE amplitudes increase rapidly, which induces EP stiff transport,[6] until the local EP gradient declines to the threshold. According to the theory of CGM, Waltz et al. propose a method by dividing the problem into two parts, namely, threshold calculation and EP redistribution. The threshold was calculated by the gyrokinetic code GYRO,[26] and a flexible and inexpensive 1D transport code ALPHA[27] was developed to analyze radial EP transport by reading the threshold calculated by GYRO. In the ALPHA code, Angioni model[28,29] is applied for turbulent transport of EP, but it is too weak to account for the measured EP transport with unstable AEs. Qualitative agreement with DIII-D diagnostic data supported the feasibility of the model for EP transport prediction. Next, a parallelized wrapper TGLFEP,[30] based on the gyro-Landau-fluid code TGLF,[31] was developed to efficiently calculate the threshold instead of using GYRO. The accuracy of TGLFEP/TGLF was confirmed by verification with GYRO[30] (error ~13% for threshold calculation) and was applied for ITER prediction.[32] Concurrently, the ALPHA code was extended to EPtran[33] by the inclusion of particle transport in phase space. We should emphasize that TGLFEP is only used to estimate the linear stability threshold. A simplified transport model EPtran (described later) is used for AE-induced transport once the threshold is exceeded.

There are other proposed critical gradient models including Ghantous et al.,[12] and Gorelenkov et al.[34,35] In our opinion, the CGM proposed by Waltz et al.[24] and the pCGM proposed by Ghantous et al.[12] are complementary. Both could serve as useful tools for scanning studies of future burning plasma experiments. Waltz's model is based on gyrokinetic/gyrofluid physics using GYRO/TGLF, whereas Ghantous' model is based on MHD/kinetic physics using NOVA-K.[36] A recent paper published by Taimourzadeh et al.[37] presented an extensive benchmarking of a number of Alfvén eigenmode stability codes including GYRO and NOVA. Despite the different physics employed by these codes, the predicted frequencies agree within 8.4%. Similar trends in the growth rate are demonstrated, and the computed values are within 26% when considering both gyrokinetic and fluid codes. We also note that the marginal stability thresholds for the two models are different. Ghantous et al. employ NOVA-K to find the most unstable AE and compute the drive from linear growth rate, while the damping is calculated using analytic expressions (or from NOVA-K). By comparing the drive and damping, the critical gradient can be calculated, i.e., marginal stability is $\gamma_{\text{drive}} = \gamma_{\text{damping}}$. Thus, the EP redistribution is induced only by AE without coupling to background modes in the method of Ghantous. Waltz et al. assumed that the marginal stability is $\gamma_{\text{AE}} = \gamma_{\text{turbulence}}$, where either GYRO or TGLF is used to calculate the growth rate for both AE and turbulence. Furthermore, γ_{AE} computed by GYRO/TGLF includes both the EP drive and the AE damping, which cannot be separated. There is also a non-perturbative nCGM proposed by Gorelenkov et al.,[34] which couples the HINST code and the kick model. This approach is more computationally intensive. It has been used to compare with Ghantous' pCGM and could be used to compare with our CGM in the future. Since there are still many issues we do not understand about EP and AE interactions, exploring different approaches to model EP physics is essential.

In this paper, we follow the simulated method of Waltz (to avoid confusion, "CGM" refers to the method of Waltz henceforth) and employ the combination of TGLFEP and EPtran, with two improvements, to predict EP transport and redistribution. First, the critical transport threshold calculation is optimized. Instead of a fixed value,[30] the local normalized EP density gradient is defined as a function that is inversely proportional to the local EP density. This represents a better one-to-one correspondence with linear stability theory. The coefficients of the function are calculated by TGLFEP. The threshold increases with the decreasing density, so that the transport function converges to a marginal level earlier than previous simulations and the EP density in saturated state in the core is thus higher. Second, since the previous CGM only considered EP loss induced by diffusion across the last closed flux surface (LCFS), during EPs' transport outward, most of the EPs are deposited at large minor radii due to collisional slowing down before they get to the LCFS. This leads to an over-prediction of the EP density in the outer region when compared with experiment. Indeed, the non-uniformity of the magnetic field leads to drifts of the guiding center, which induces EP orbit losses in the outer region. To account for this, the ORBIT code[18] is employed to calculate the trajectories of guiding centers and identify the EP loss cone in phase space. Importantly, the modification of the loss cone by unstable AEs is also included, however, the effect of the loss cone on AE stability is neglected. FLR effect is not included in ORBIT simulation.

In addition, the thermal plasma evolution is neglected since the diffusivity of EP is much larger than that of the bulk plasma, and we cannot consider EP nonlinear effects due to the limitations of the linear code TGLFEP.

The DIII-D discharges, #142111 with reverse magnetic shear[38] and #153071 with monotonic q-profile,[39] are selected to verify the improvements. For each case, we focus on the equilibrium at a single extensively analyzed time slice, i.e., 525 ms for #142111 and 3310 ms for #153071. The initial EP distribution is obtained by TRANSP[40] without radial diffusion (classical slowing down), and EP transport is assumed to be induced by a single Toroidal Alfven Eigenmode (TAE) (the most unstable n) on each surface. The loss fraction, deposited profile, and effective diffusivity calculated by the improved CGM are compared with experiments. For the two discharges, the EP pressure profile was obtained by kinetic magnetic reconstruction of the experimental equilibrium (by subtracting the thermal pressure from the Motional Stark Effect (MSE) constrained equilibrium pressure profile).[5,39] For both discharges, the reconstructed EP profiles are consistent with measurements.[39]

The comparison with the MEGA results is carried out in three parts. First, the predicted linear growth rates and unstable AE regions are benchmarked. This is followed by a comparison of the AE redistributed profiles for discharge #142111. Finally, based on the agreement between these profiles, a detailed evaluation of the MEGA nonlinear stability thresholds for a single (most unstable) mode and multi-modes are compared with the CGM transport threshold. Specifically, the critical density gradients for both models are analyzed in detail and the difference with the AE linear stability threshold is quantified.

As an application, EP redistribution is predicted for a CFETR steady state scenario by the improved CGM. Three transport mechanisms, namely, background turbulent transport, radial transport induced by unstable AEs, and losses due to finite orbit width (FOW) effect, are discussed. The contribution of each mechanism is separately analyzed and also evaluated in combination. The key factors leading to enhanced losses are identified.

The paper is organized as follows: Section II explains the simulation method for AE stability and EP transport. Section III describes the improvement of the CGM, which is benchmarked with two DIII-D discharges and with the MEGA results in Sec. IV and in Appendix A. Applying the same model, Sec. V discusses the prediction for a CFETR steady state scenario and analyzes the dominant AE effects on alpha particle losses. Finally, the conclusions are presented in Sec. VI.

II. SIMULATION METHOD
A. AE stability and critical gradient

In this paper, four codes are employed. TGLFEP is used for local AE stability, MEGA is for global AE stability, ORBIT is employed to calculate loss cone, and EPtran is used for EP redistribution. To be consistent with the data format of EPtran, MEGA and ORBIT results are only focused on the profile of low field side midplane.

MEGA is a magnetohydrodynamic (MHD) kinetic hybrid code,[41] using an assumption that the EP density is much less than the bulk plasma density. Nonlinear MHD equations are employed to describe the bulk plasma, and the EPs are simulated with the δf method.[42,43] The contribution of EPs is added into the MHD momentum equation through a term representing the EP current density.

The EP current density includes the contributions from parallel velocity, magnetic curvature drift, magnetic gradient drift and magnetization current, while the $E \times B$ drift due to quasi-neutrality is neglected. The code employs (R, φ, z) coordinates and the shape of the outermost magnetic surface is circular. In this paper, we use the MEGA code to benchmark a revised CGM, such as the radial width of AE mode, linear growth rate and critical gradient, and the redistributed EP profile.

TGLF is a gyro-Landau-fluid code developed to reproduce the turbulent physics of a gyro-kinetic code, such as GYRO. It has two parts, namely, a stability code and a turbulent transport module. Both have been extensively calibrated against linear and nonlinear GYRO simulations.[26] TGLFEP follows the philosophy of TGLF by extending the stability physics to include EPs. In our CGM, TGLFEP is only used to calculate the stability properties of the AE modes. AE-induced EP transport is modeled by a simplified code EPtran, which uses the TGLFEP predicted stability threshold to guide EP transport modifications. Unlike the transport module in TGLF, which consists of an elaborately derived quasilinear weighting factor and saturation rule, the transport coefficient in EPtrans is based on a few simple assumptions described in Sec. II B.

In TGLF, to solve a set of moment equations (density, parallel velocity, parallel pressure, total pressure, parallel energy flux, and total energy flux equations), the eigenfunctions are represented by a set of Hermite basis functions. The number of basis functions is raised to 32 from the default value of 4 for AE stability analysis from past experience. Since the TGLFEP simulation result is sensitive to the Gaussian width θ_w of the basis functions,[30,31] an appropriate width needs to be ascertained for the maximum growth rate. Instead of automatic selection, we scan the Gaussian width in a range, e.g., 0.4–2.0 for discharge #142111, for an optimal value. Our criterion is that both the frequency and growth rate have to show robustness over a range of Gaussian width (with the increased set of basis functions). Figure 1 displays (a) the growth rate and (b) the frequency of three n = 3 modes for the stated Gaussian width range. The orange and purple curve represent TAEs, since the growth rate and frequency maintain roughly the same values over a wide range of Gaussian width. On the other hand, the blue curve has a strong perturbation, and outgoing boundary condition[44,45] is not satisfied. Therefore, we consider this result as polluted by numerical noise and neglect it in the simulation. The growth rate and frequency computed by MEGA under the same conditions are indicated by black lines in the corresponding figures. Comparing the orange curve with the MEGA result, the maximum error is at $\theta_w = 0.4$ obviously (24% for growth rate and 46% for frequency). The orange curve keeps flat within $\theta_w = 1$–2. In this range, the error of frequency is 7%–18% and mean error of growth rate is 7%. TGLFEP is a parallel wrapper code of TGLF constructed to find the suitable Gaussian width and calculate AE frequency and growth rate in multiple flux surfaces automatically. The method of the critical gradient calculation is improved by careful consideration of the threshold evolution, which will be discussed in Sec. III A.

B. EP transport

Once the critical gradient profile is known, the EP redistribution can be calculated by the EPtran code. The transport equation for the EP distribution function can be written as
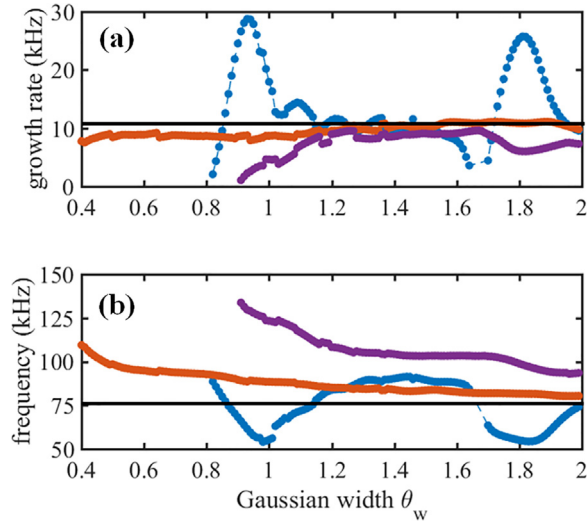
FIG. 1. (a) Growth rate and (b) frequency as a function of Gaussian width. The orange and purple curves represent acceptable TAEs calculated using TGLFEP. Because the blue curve has a strong perturbation, the mode is treated as polluted by numerical noise. For comparison, the MEGA results are depicted by the black lines.

$$\frac{\partial f_{EP}}{\partial t} + \frac{1}{V'}\frac{\partial}{\partial r}(V'\Gamma^r) + \frac{1}{V^E}\frac{\partial}{\partial E}(V^E\Gamma^E)$$

$$= \frac{2}{\tau_s\sqrt{E}}\frac{\partial\left[\left(E^{3/2}+E_c^{3/2}\right)f_{EP}\right]}{\partial E}$$

$$+ \frac{S_0}{2\pi\sqrt{E}}\delta(E-E_0) + \nu_d\frac{\partial}{\partial\xi}\left(1-\xi^2\right)\frac{\partial f_{EP}}{\partial\xi}, \quad (1)$$

$$\Gamma^r = -D_{EP}^{rr}\partial f_{EP}/\partial r - (T_{EP}/a)D_{EP}^{rE}\partial f_{EP}/\partial E, \quad (2)$$

$$\Gamma^E = (T_{EP}/a)D_{EP}^{Er}\partial f_{EP}/\partial r - (T_{EP}/a)^2 D_{EP}^{EE}\partial f_{EP}/\partial E. \quad (3)$$
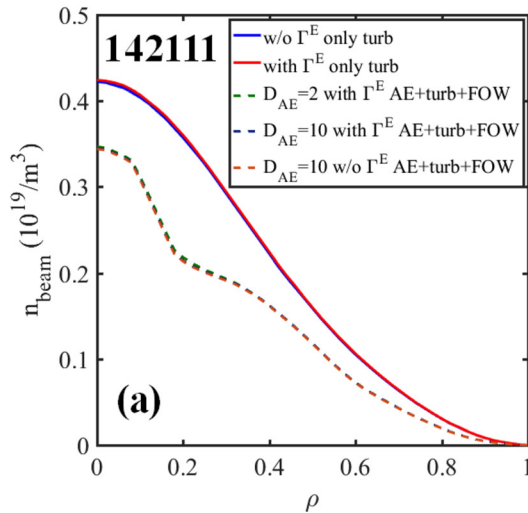
The right hand of Eq. (1) includes the slowing down term, source term and pitch-angle scattering term[46] for neutral beam (NB) or alpha particles. In the equations, r is radial location, E is EP energy, S_0 is the strength of the EP source, E_0 is the initial energy for EP (3.5 MeV for alpha particle or injected energy for NB), τ_s is the slowing down time, E_c is the crossover energy, T_{EP} is equivalent Maxwellian temperature, a is minor radius, V is plasma volume, and ν_d is pitch angle scattering rate.[46] $V' = \partial_r V$, $V^E = 1/\sqrt{E(1-\lambda)}$, $\xi = \sqrt{1-\lambda} = v_{\parallel}/v$ and magnetic moment $\lambda = \mu B/E$. As labeled on the outboard side, particles with $0 \le \lambda < \lambda_{TP}$ correspond to passing particles and $\lambda_{TP} \le \lambda \le 1$ to trapped particles with $\lambda_{TP}(r) = B(0)/B(\pi)$.[47] Equation (1) is solved at the bottom of the magnetic well on each flux surface, i.e., along the outer midplane. This is the location where all particles will pass through. The collision operator acts to change the pitch-angle and energy of each particle, and the turbulent operator leads to energy change and radial diffusion. Knowing a particle's change in (r, v) space, orbit theory can inform us whether the particle moves from passing to trapped, and specifically if it enters a loss cone. Thus, Eq. (1) provides key information on the change in EP profile as well as enhanced losses due to the presence of loss cones. The simulation indicates that the redistribution profile is insensitive to the energy diffusion, Γ^E. Figure 2(a) represents the redistribution profile only with background turbulence, and includes AE. Energy diffusion changes the EP distribution in phase space, especially for low energy particles, but it only slightly affects the integrals of f_{EP} in the density and effective temperature calculations. For completeness, we have added energy diffusion for computing the EP distribution.

Equations (2) and (3) employ a 2×2 diffusivity matrix according to Ref. 47. In the matrix, the diffusion coefficient D_{EP}^{rr} that describes the EP transport induced by unstable AEs is originally expressed as

$$D_{EP}^{rr} = D_{AE}\left(\frac{a}{n_{EP}}\right)\left[\left(-\frac{\partial n_{EP}}{\partial r}\right) - \left(-\frac{\partial n_{EP}}{\partial r}\right)^{th}\right]_{>0} + D_{ITG/TEM}, \quad (4)$$
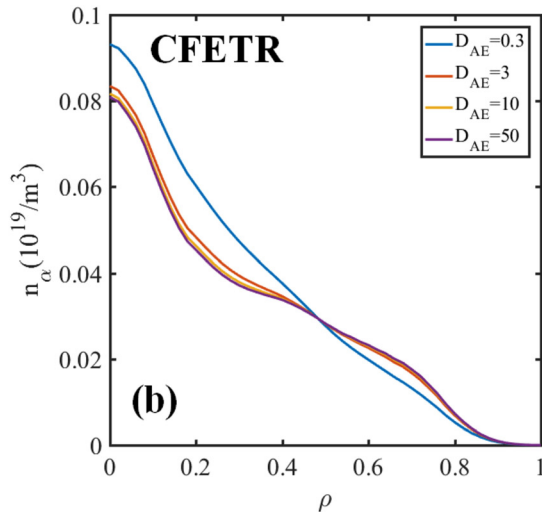

FIG. 2. (a) Radial profiles of EP redistribution for DIII-D #142111. Solid curves depict EP redistribution by only background turbulence without Γ^E (blue) and with Γ^E (red). Dash curves depict EP redistribution by both turbulence and AE without Γ^E (blue) and with Γ^E (red), and $D_{AE} = 2$ is depicted by the green dash curve for comparison. Only the most unstable $n = 3$ AE mode is considered for this comparison. (b) Γ particle redistribution with D_{AE} value of [0.3, 3, 10, 50] for CFETR.

where $[x]_{>0} = 0$ if $x < 0$, and $-(\partial n_{EP}^{th})/\partial r$ is the local critical density gradient. D_{AE} is not from any physical estimation. It is set sufficiently large to rapidly drive the EP density gradient close to the threshold to mimic a critical gradient phenomenon. This is supported by a recent paper[48] which estimated the magnitude of D_a to be ~ 1–10 m²/s compared with typically ~ 0.1 m²/s for the background. In previous investigations, D_{AE} was set as 0.3 for ITER[27] and 10 for DIII-D experiment.[24] Indeed, the redistributed profile is insensitive to a range of D_{AE} values. In Fig. 2(a), the blue curve and green dashed curve show hardly any difference in the modified profiles with two very different D_{AE} values for a particular DIII-D discharge scenario. Figure 2(b) depicts α particle redistribution with D_{AE} value of [0.3, 3, 10, 50] for CFETR. The profiles are quite close (error $<5\%$) except for $D_{AE} = 0.3$. Thus, following the published paper, we set $D_{AE} = 10$ for the two DIII-D experiments, and for CFETR we set $D_{AE} = 3.0$. Both are in the range where the redistributed EP profile is insensitive to D_{AE}.

The diffusivity matrix is positive definite and symmetric with $D_{EP}^{rE} = D_{EP}^{Er} = -A_{EP}D_{EP}^{rr}$, and $D_{EP}^{EE} = A_{EP}^2 D_{EP}^{rr}$. A_{EP} is a function of the EP temperature, and the formula is expressed in Appendix A 3 of Ref. 30. For DIII-D cases, A_{EP} is often lower than 1. $D_{ITG/TEM}$ is the background micro-turbulent diffusivity according to the Angioni model (Appendix B), in which helium ash and EPs have different diffusion coefficients.[27] Both energy-independent and energy-dependent models are described in Appendix A of Ref. 33 as well. The comparison between the two models based on DIII-D discharge #142111 is depicted in Fig. 3, where ρ represents the square root of toroidal magnetic flux, and D_α is the equivalent diffusion coefficient $[D_\alpha(r) = (\int \Gamma^r(r,E) \ dE)/(dn/dr)]$. As shown, the energy-dependent diffusivity is lower inside and larger outside in comparison with the energy-independent diffusivity, and the ratio can be fitted by a cubic polynomial approximately. The energy dependent model is used for our paper, but the difference between the two models should be small.

According to the expression of AE growth rate in Ref. 49, the diffusivity is rewritten as
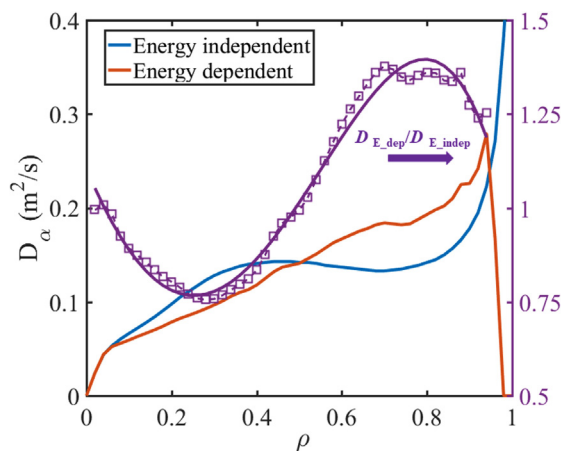

FIG. 3. Comparison between energy-dependent (orange) and energy-independent (blue) Angioni diffusion coefficients. The ratio of the two coefficients is depicted by purple squares, which are fitted by a cubic polynomial (purple curve).

$$D_{EP}^{rr} = D_{AE}\left[\left(\frac{a}{L_{nEP}}\right) - \left(\frac{a}{L_{nEP}}\right)^{th}\right]_{>0} + D_{ITG/TEM}, \quad (5)$$

where L_{n_EP} means the characteristic length of EP density $[L = n/(dn/dr)]$. This form will be justified in Sec. III A.

The EP distribution f_{EP} is calculated by evolving Eq. (1), and the EP density and equivalent Maxwellian temperature can be expressed as moments of f_{EP}

$$\left[n_{EP}, \frac{3}{2}n_{EP}T_{EP}\right] = \frac{1}{4}\sum_{\sigma=\pm 1}\int_0^\infty 2\pi\sqrt{E}dE \int_0^1 \frac{1}{\sqrt{1-\lambda}}[1, E]f_{EP}, \quad (6)$$

where $\sigma = \pm 1$ means along/against the direction of magnetic field.

The initial distribution is set as the classical slowing down distribution,

$$f_s(r, E) = \frac{S_0\tau_s}{4\pi}\frac{H(E-E_0)}{E^{3/2}+E_c^{3/2}}. \quad (7)$$

Following Eq. (6), the density profile is $n_{sd}(r) = S_0\tau_s I_2(v_c/v_0)$, and the equivalent Maxwellian temperature profile is $T_{sd} = (2I_4/3I_2)E_0$. The integral function is defined as $I_n(a) = \int_0^1 x^n dx/(a^3 + x^3)$. For alpha particles, S_0 is obtained from the fusion reaction rate calculated using the background plasma properties according to the D-T reaction cross section. For the Neutral Beam Injection (NBI) case, S_0 is the initial NB ion source given by NUBEAM.[50] The classical slowing down distribution is obtained by solving Eq. (1) with only the collisional operator and S_0. Here, the source term S_0 is treated as only the full-energy component of the NB source in EPtran.

III. IMPROVEMENT OF CRITICAL GRADIENT MODEL

First, we summarize the major changes. The CGM is improved by detailed accounting of the threshold evolution and orbit loss mechanisms, which were not considered in the original model. The threshold is modified to be the normalized critical gradient (a/n dn/dr) instead of the critical gradient (dn/dr). Furthermore, we relate the new threshold to the EP density by the TGLFEP code, which closely reflects the form from previous theory. Meanwhile, in the EPtran code, we define an EP loss cone, which is calculated by the ORBIT code. The loss cone provides an additional loss channel away from the LCFS for EPs with finite orbits (the particle drifting beyond the LCFS is defined as "loss" in this paper). This turns out to be non-negligible in the presence of AE-induced transport and is particularly important for lower current discharges. In this paper, we ignore Finite Lamor Radius (FLR) effect, which would expand loss cone slightly. The two improvements lead to a significant reshaping of the EP profile, bringing a much closer agreement with experiment.

A. Threshold evolution

In Refs. 24 and 51, Waltz and Bass discussed various recipes of marginal stability, which is introduced in Appendix A in detail. In this work, we employ the recipe of $\gamma_{AE+ITG/TEM} = \gamma_{ITG/TEM}$ for marginal stability, where $\gamma_{AE+ITG/TEM}$ means growth rate of AE considering background plasma, and $\gamma_{ITG/TEM}$ means growth rate of turbulence. TGLF employs an equivalent Maxwellian distribution for EP, so that the growth rate is an approximation. The comparison of local growth rate between using Maxwellian and slowing down distribution by

GYRO is exhibited in Ref. 24. We note from Eq. (5) that when (a/L_{nEP}) equals the critical gradient $(a/L_{nEP})^{th}$, AE-induced transport is turned off and the EP profile will reach a saturated state. The key issue of the CGM is the proper definition of the critical gradient. Since TGLFEP is a local stability analysis code, the critical gradient is calculated for each flux surface. In previous CGM simulations, the characteristic length of EP density (L_{nEP}) was assumed to be fixed.[30] In searching for the critical gradient $-(\partial n_{EP}^{th})/\partial r$, the authors would reduce the EP density (with density gradient decreasing proportionally) until the growth rate calculated by TGLFEP equals the growth rate of the background turbulence. The density gradient at this point is defined as the critical density gradient [see Eq. (4)]. Obviously, the assumption means the shape of the density profile remains fixed, which is not consistent with experiment. Although a correction factor was added,[30] the profile was modified little. Furthermore, an artificial parameter is needed as an input for the correction. If instead, we perform a more complete two-dimensional $(a/L_{nEP}, n_{EP})$ search of the critical normalized gradient $(a/L_{nEP})^{th}$ using TGLFEP, one finds that $(a/L_{nEP})^{th}$ actually increases with decreasing n_{EP} (Fig. 2). The choice of a constant (a/L_{nEP}) assumed in the previous CGM appears to be arbitrary and overly restrictive. To relax this assumption, we resort to an analytic formula of AE growth rate,[49]

$$\frac{\omega_i}{k_\parallel v_A} = -q_0 \left(\frac{\beta_c}{2} \left(G_{mi}^T + G_{me}^T \right) + \beta_\alpha \left(G_{m\alpha}^T - n q_0 \delta_\alpha H_{s\alpha}^T \right) \right), \quad (8)$$

where ω_i is the growth rate, $k_\parallel$ is the parallel wave number, v_A is the Alfvén velocity, q_0 is the local safety factor, β_c is the beta of bulk plasma, β_α is the beta of EP, n is the toroidal mode number, $\delta_\alpha = -(2/3) r_{L\theta} (dp_\alpha/dr)/p_\alpha$, $r_{L\theta} = v_\alpha/(q_\alpha B/m_\alpha)$. v_α, q_α, and m_α are the velocity, charge, and mass of EP. The functions G and H are described by Eqs. (67) and (70) of Ref. 49. The first term on the RHS represents Landau damping of bulk ions and electrons, which are constant in linear phase by assuming the background equilibrium to be fixed during EP transport. The second term includes damping and drive of EP, where only β_α and δ_α [$\propto dp_\alpha/(p_\alpha dr)$] will be modified during EP transport. Since the EP drive term explicitly contains both pressure and pressure gradient, we should also allow L_{nEP} to vary as the EP profile evolves from unstable AE to marginally stable AE (which is also inferred in Ref. 12). Therefore, we adopt the normalized density gradient a/L_{nEP} to investigate marginal stability instead of density gradient (dn_{EP}/dr). For marginal stability, Eq. (8) can be rewritten as

$$\frac{a}{L_{nEP}^{th}} = \frac{k_1}{n_{EP}} + k_2, \quad (9)$$

where k_1 represents Landau damping of bulk plasma and k_2 is the Landau damping of EP itself as well as the temperature gradient drive of EP. The two parameters are constant at each surface by neglecting temperature modifications. Thus, we can obtain the critical a/L_{nEP} as an inversely proportional function of EP density in each flux surface by TGLFEP. In principle, we could compute the critical threshold for each time step without making this simplification, which would take much longer computation time. Here, we just focus on the $n = 3$ mode and will discuss the case with multiple n in Sec. IV A. Figure 4(a) plots the critical a/L_{nEP} profile with initial n_{EP}, i.e., without EP transport, by the dashed red curve. The solid black curve represents a/L_{nEP} of the classical slowing down distribution. When the black

curve exceeds the threshold (indicated by the shaded region), AEs are unstable according to Eq. (5). For the unstable region, critical a/L_{nEP} can be determined by k_1 and k_2 as plotted in Fig. 4(b) for several radial locations. The circles are outputs of TGLFEP by density scanning and fitted by dashed curves with the corresponding colors, respectively. The upper right region of the curve represents the AE unstable region, and the lower left region of the curve represents the AE stable region. As the transport equation [Eq. (1)] is evolved and EPs diffuse outward, EP density decreases in the core, therefore the threshold increases. The critical threshold of $\rho = 0.4$ is enlarged in Fig. 4(c), and the initiation point (before transport) is depicted by a red cross. The normalized density gradient a/L_{nEP} follows the red arrow trajectory to reach marginal stability (since a/L_{nEP} is allowed to change). In comparison, the black arrow represents the trajectory of the old CGM. Clearly, there could be a significant difference in the EP profile between the two models. It is important to point out that the critical gradient defined in this section does not correspond to the linear stability threshold. It is larger because of the gradient needed to balance the background turbulence induced EP transport.

B. Loss cone due to finite orbit width (FOW)

Since the previous CGM only considers EP losses induced by diffusion at the LCFS, few EPs are lost, and instead, most of the EPs settle at larger minor radii. Not being considered, however, is the non-uniformity of the magnetic field that leads to non-negligible drifts of the guiding center orbits. In fact, at the high energies under consideration, the FOW of the EPs in the outer region of the plasma can easily intersect the LCFS resulting in additional orbit losses of fast particles, which was measured in experiment.[38] Clearly, this needs to be included in the improved CGM. Following the method described in Ref. 5, the ORBIT code is selected to calculate the loss boundary and construct a loss cone in (ρ, E, ξ) space.

The initial EP distribution is chosen to be a uniform distribution in (ρ, E, ξ) space, and all particles are located at the outer midplane. Because the ORBIT code employs 2D (R, Z) spatial coordinates, restricting the consideration to the outer midplane (low magnetic field side) reduces the number of test particles and therefore reduces simulation time. Certainly, the lost fraction of EPs is overestimated with this choice, since the particles are more susceptible to losses on the low magnetic field side. If we set initial particles at the inner midplane (high magnetic field side), the loss cone is approximately halved.

In addition, the lost fraction of EPs increases and the loss cone expands by including AE perturbations. For example, by using the parameters of DIII-D discharge #142111, we depict two obvious cases for a variety of orbit trajectories in Fig. 5(a) for trapped particle and Fig. 5(b) for counterpassing particle. The blue thick curve indicates the trajectory without AE, and red thin curve indicates the trajectory with AE. Here, the AE means $n = 3$ TAE, and the structure will be exhibited in Sec. IV A. The initial state for testing particle is $\rho = 0.6$, $v_\parallel/v = -0.46$, $E = 40$ keV for trapped particle, and $\rho = 0.75$, $v_\parallel/v = -0.78$, $E = 62$ keV for passing particle. To distinguish the variety of trajectories clearly, the amplitude is set as $O(10^{-3})$, which is larger than experimental AE amplitude of $O(10^{-4})$. The trajectory of passing particle on the high magnetic field side is enlarged in Fig. 5(c). For each case, black cross marks the initial position of testing particle, and red cross marks the position where particle escapes from the LCFS. The black arrow represents particle moving direction. We note
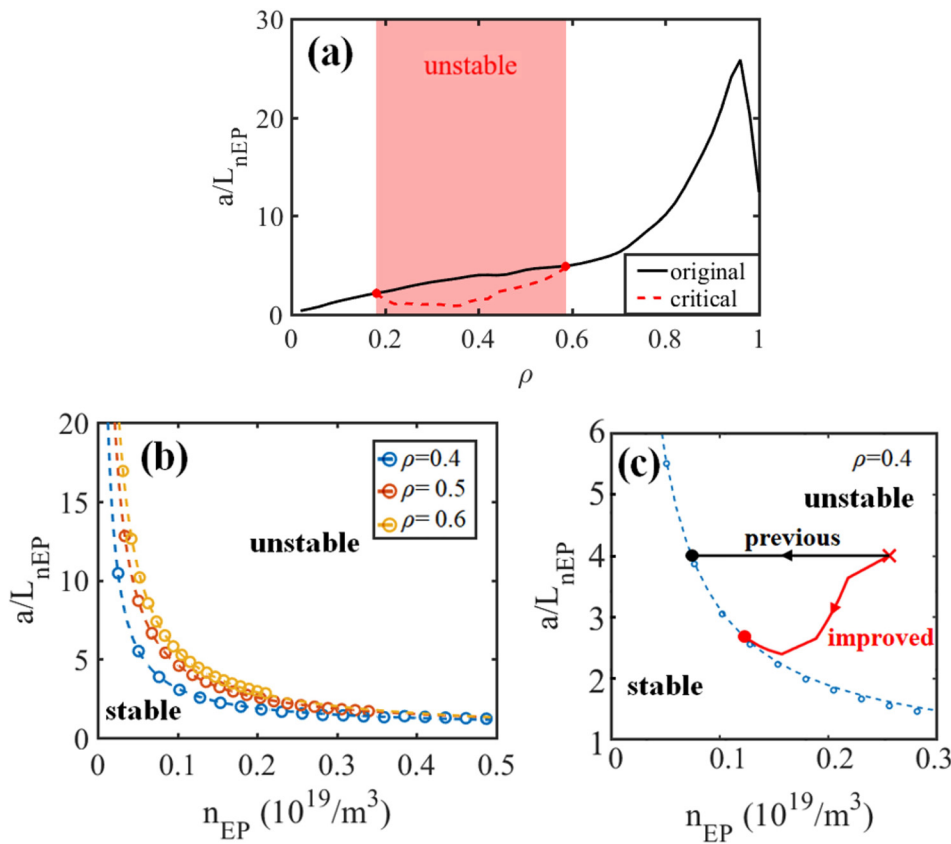
FIG. 4. (a) Unstable AE region of $n = 3$ without transport. Critical a/L_{nEP} is depicted by dashed red curve, and a/L_{nEP} of classical slowing down distribution is depicted by solid black curve. (b) Inverse proportional function between critical a/L_{nEP} and n_{EP} at $\rho = [0.4\ 0.5\ 0.6]$. (c) Density evolution trajectories of previous CGM (black) and improved CGM (red) at $\rho = 0.4$.
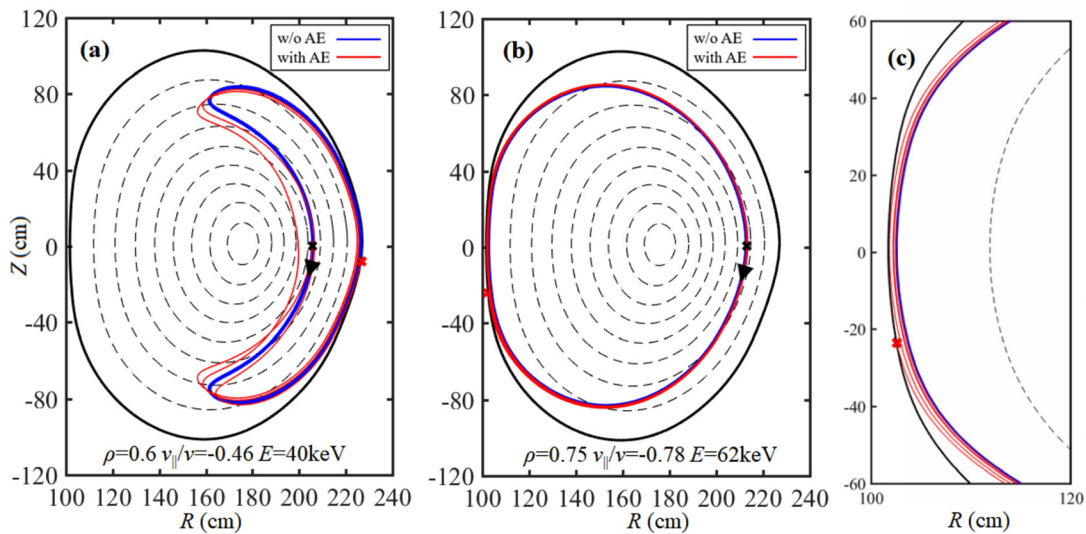

FIG. 5. Representative trajectories of (a) trapped and (b) counterpassing particles by including AE perturbation. The energies are chosen from illustrative NB particles in DIII-D discharge #142111. Blue thick curves depict the trajectories without AE, and red thin curves depict the trajectories with AE corresponding to the unstable region in Fig. 4(a). Black cross marks the initial position of testing particle, and red cross marks the position where particles escape from the LCFS. The black arrow represents the particle moving direction. The initial state of testing particle is exhibited in each plane. AE amplitude is set as $O(10^{-3})$. The high magnetic field side of (b) is enlarged in (c) to reveal trajectory variations.

that in the pCGM of Ghantous,[12] FOW effect is also included for EPs that are affected by the unstable AE by directly following their orbits.

Figure 6(a) indicates the loss boundaries of multiple energies without AE perturbations. The loss region is on the right side of each curve. Since the initial particles are selected at the outer midplane, all lost particles have negative pitch-angle (pitch-angle is relative to the direction of Ip for #142111). The loss cone enlarges with increasing energy. For the particles with injection energy (80 keV), the peak of loss cone approximately touches the axis. Furthermore, the loss cone expands in the core by including AE [Fig. 6(b)], and a small loss cone also appears for particles with positive pitch-angle. Here, the AE amplitude is set to dB/B ~ $O(10^{-4})$ according to data from publications.[5,38] The loss cone is input into EPtran to account for EP losses inside LCFS, and the EP distribution is taken to be zero in this region.

IV. VALIDATION OF THE IMPROVED CGM

With the improvements, we establish a workflow to calculate the EP distribution using multiple codes. The EFIT code[52] is employed to reconstruct the experimental equilibrium, which is used by the other codes. The TGLFEP code calculates the local threshold for AE marginal stability. The toroidal mode number for the most unstable mode can vary across the minor radii. The global mode structure is obtained by the MEGA code, and the AE magnetic perturbation is input into the ORBIT code for loss cone calculation. Both the threshold and loss cone are read by the EPtran code for EP redistribution predictions.

Two DIII-D discharges (#142111 and #153071) are selected to confirm the improved CGM. Low n (n = 1–5) TAEs are always destabilized in discharge #142111, and n = 2–4 Reversed Shear Alfven Eigenmode (RSAEs) are also driven unstable when the minimum of q (q_{min}) is further decreased as the discharge evolves. For convenience, the equilibrium at t = 525 ms is selected without unstable RSAE, because q_{min} is a bit greater than $m/n = 4$ at this time. This condition is unfavorable for RSAE existence. In discharge #153071, TAEs with ~100 kHz are destabilized due to a monotonic q-profile. Since AE activities change little within 3200–3700 ms,[53,54] we select 3310 ms for our EP transport study. The two discharges have similar main plasma parameters in the chosen time slices: B = 2 T, I = 0.74 MA, R = 1.7 m and a = 0.6 m for discharge #142111, and B = 1.77 T, I = 0.9 MA, R = 1.8 m and a = 0.6 m for discharge #153071. The electron density, safety factor, pressure of thermal particle, and EP (classical slowing down) profiles are depicted in Fig. 7, in which blue curves are for #142111 and red curves are for #153071. In Fig. 7(c), solid curves depict the background plasma pressure and dashed curves depict the EP pressure.

A. Discharge #142111

Low n TAEs with frequency of 70–90 kHz are measured by ECE at 525 ms (Fig. 4 of Ref. 51). These modes are overlapping and located around ρ ~ 0.4. The evolution of energy for n = 1–5 TAEs calculated by MEGA is plotted in Fig. 8(a). The most unstable mode is n = 3 TAE, which saturates first and its energy is significantly higher than the other modes. The mode structure in linear state, corresponding to the red dashed line of Fig. 8(a), is depicted in Fig. 8(b). Consistently, Fig. 9(a) displays the results of local code TGLFEP, which indicates that the growth rate of n = 3 is the largest across the mode width computed by MEGA, but n = 1–4 modes are dominant successively from ρ = 0.1 to ρ = 0.6. Hence, EPtran simulates the EP redistribution based on the minimum critical gradient of the n = 1–4 modes obtained from TGLFEP across the same minor radii. The critical a/L_{nEP} profile is depicted by the purple line in Fig. 9(b), and for comparison, we also plot the original and n = 3 profiles, which are the same as in Fig. 4(a). The overlap of purple and orange circles from ρ = 0.2–0.6 indicates that n = 3 is dominant over a broad region of the plasma, except for ρ < 0.2. Obviously, the threshold should be calculated by evaluating the most unstable n for each flux surface for accuracy. In addition, the sensitivity of the critical gradient for single n in the presence of other modes will be further elaborated in Appendixes A and B.

In the EPtran code, the EP pitch-angle distribution was previously set as a Gaussian function without countermoving particles [Eq. (6) of Ref. 33]. However, as indicated by the ORBIT code, the particle loss region is much larger for countermoving particles and peaks around $v_{||}/v \approx -0.5$ (Figs. 8 and 18 of Ref. 5). Furthermore, even with a co-moving injected beam, the population of countermoving particles
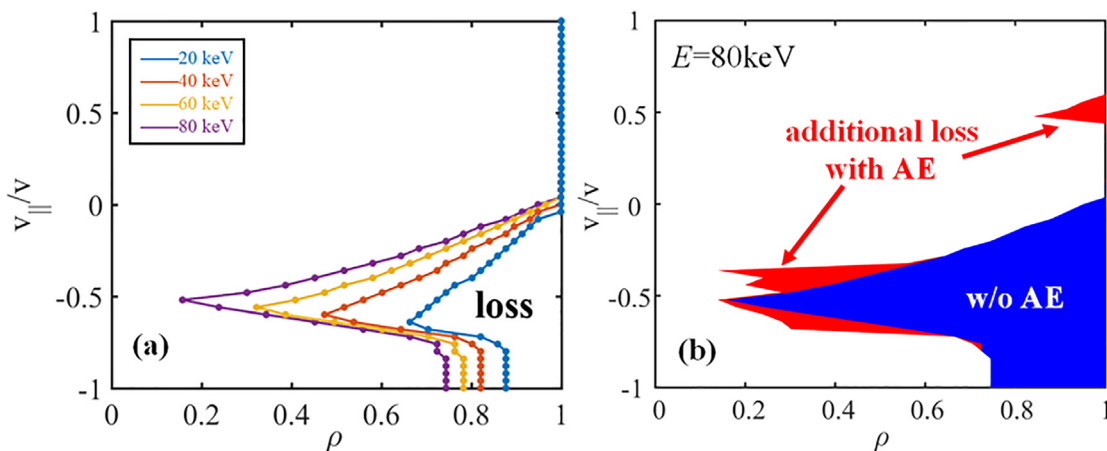

FIG. 6. (a) Loss boundary in (ρ, v||/v) space with different energies. ORBIT results are depicted by points, which are connected by the corresponding solid curves. The loss region is on the right side of the curve. (b) Loss cone without/with AE perturbation. The blue area represents the loss cone without AE, and the additional loss by including AE is highlighted by the red area.
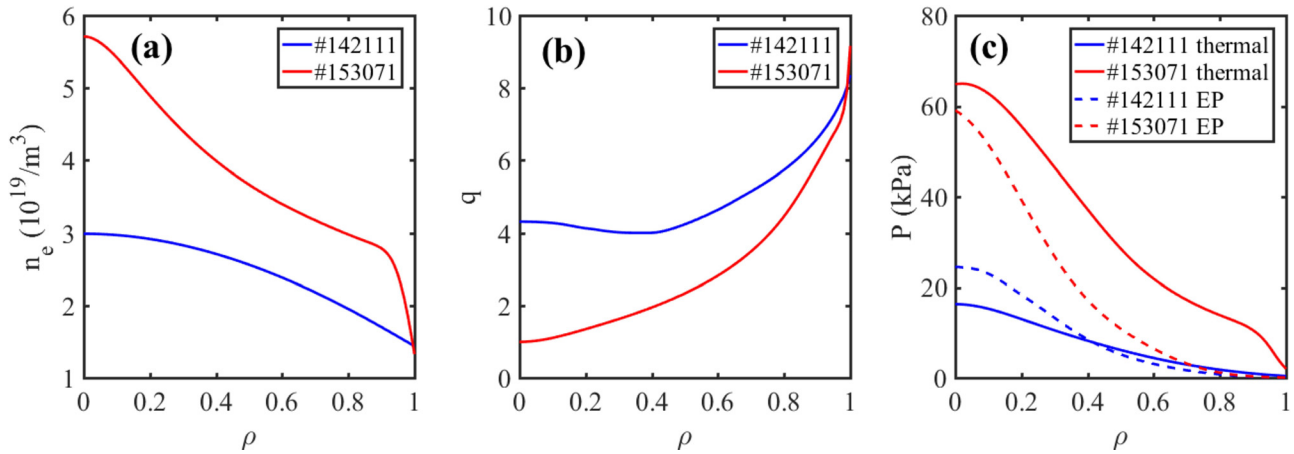
FIG. 7. Plasma profiles of discharges #142111 (blue) and #153071 (red), (a) electron density (b) safety factor (c) pressure, dashed curve represents EP pressure, which is calculated by classical slowing down distribution without transport.

becomes finite quickly. This is because Coulomb collisions can cause non-negligible transfer of EPs from the positive direction to the negative direction. TRANSP shows EPs locate in negative pitch-angle space obviously (Fig. 11 of Ref. 5). Thus, we have to add the EP distribution with negative pitch-angle to account for the pitch angle scattering effect as

$$f(\xi) = \exp\left(-(\xi - \xi_0)^2/\Delta\xi^2\right) + k_{pitch}\exp\left(-(\xi - \xi_0)^2/\Delta\xi^2\right). \quad (10)$$

The distribution function in negative pitch-angle space refers to previous function with positive pitch-angle. The location of the peak is set as $\xi_0 = 0.6$, the width is set as $\Delta\xi = 0.2$, and the peak with negative pitch-angle is set half of peak with positive pitch-angle (Here, $k_{pitch} = 0.5$ is according to the EP distribution with 60 keV in the classical phase of MEGA (Fig. 7 of Ref. 55). These coefficients are assumed for all energy. In fact, the location is kept fixed for different energy, but the width is larger for lower energy particles.

With the two improvements described in Sec. III, the transported NB radial density profile is indicated by the purple curve in Fig. 10(a). For comparison, the classical slowing down (before transport) without FOW distribution is depicted by the black solid curve, and the experimental profile is given by the red curve, which is inferred by subtracting the thermal pressure from the total pressure in the kinetic equilibrium reconstruction under MSE constraint.[56] We also show in the same figure the prediction by the original CGM without loss cone effect (blue), as well as a prediction with the improved CGM but with a loss cone from unperturbed orbits only, i.e., no AE modification (green). The improved CGM result is much closer to the experimental profile than the original CGM. By defining the loss fraction as the ratio of loss to the classical slowing down distribution, the improvements increase EP loss fraction from 15% to 42%, which is in good agreement with the experiment (loss fraction ~50%). The density profile is no longer abnormally flat in AE region, and the EPs are lost due to the
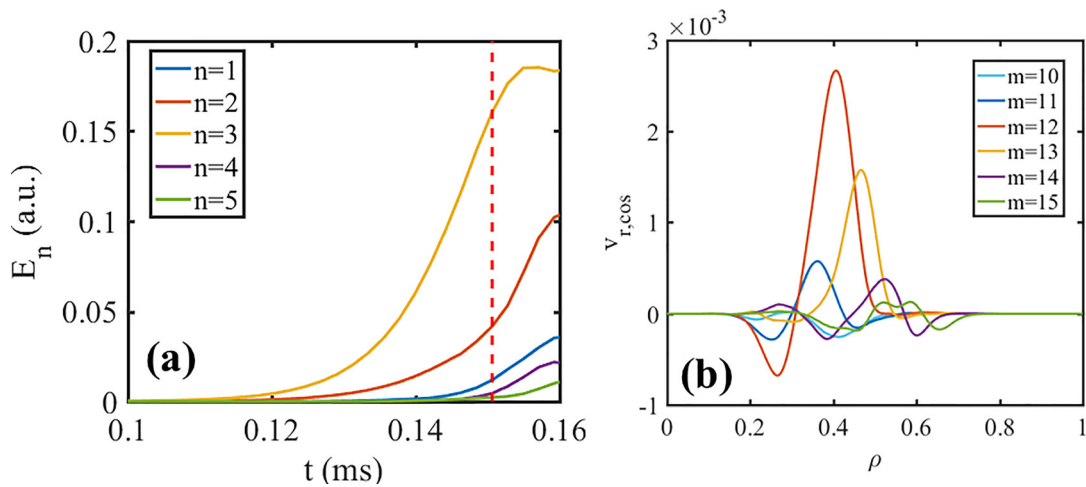

FIG. 8. (a) Evolution of energy with n = 1–5 TAEs by MEGA. (b) Cosine part of radial velocity for the most unstable n = 3 TAE. Color-coded poloidal mode number is shown in the legend, in which m = 12 and m = 13 harmonics are dominant.

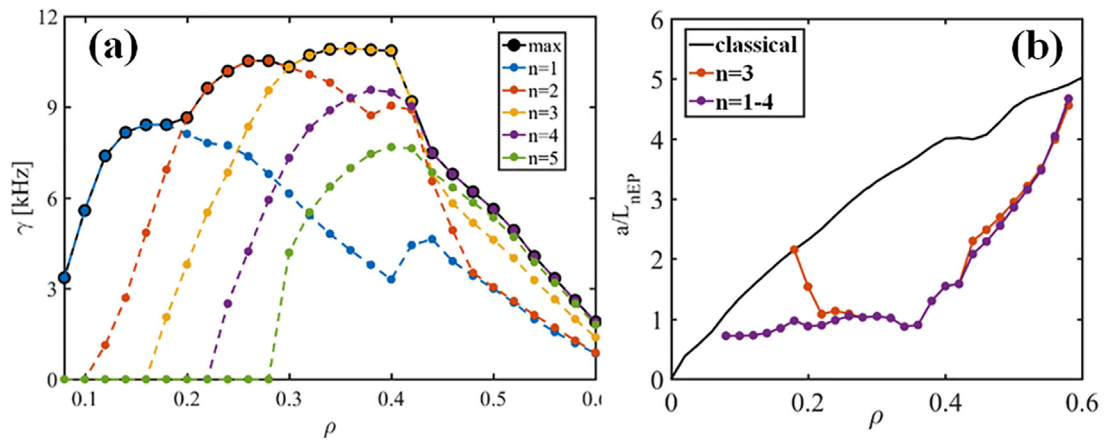**FIG. 9.** (a) n = 1–4 growth rate in each flux surface by TGLFEP. (b) Critical a/L_{nEP} profiles with n = 1–4 and n = 3 are depicted by the purple and red curves, respectively. The a/L_{nEP} of a classical slowing down distribution is depicted by the black curve.

FOW effect instead of being deposited near the edge as in the original CGM prediction. The simulation indicates that the unstable AE directly affects the EP redistribution through enhanced transport, and it indirectly contributes to increasing the EP orbit losses by modifying the FOW loss cone. The loss cone is wide at the larger minor radius. The radial transport by AE pushes the EPs outward into the loss cone, and the particles promptly escape when the orbits intersect with the LCFS. Due to finite difference method and boundary condition, the densities of the first two grid points are inaccurate and could lead to a 20% error, therefore we terminated the CGM simulations at $\rho = 0.1$ and extended the purple and green curves to the magnetic-axis using the gradients at that point. This does not affect our analysis and conclusion. In Fig. 10(a), the saturated EP profile from the improved CGM is compared with the corresponding profile from MEGA

(yellow) as well, which exhibits close agreement starting from the inner edge of unstable AE ($\rho = 0.1$, where n = 1 is the most unstable) all the way to the plasma edge. Here, the MEGA profile is from Ref. 17. The agreement in saturated profiles suggests that the two different transport models have similar EP critical threshold gradients. Since the linear growth and nonlinear saturation of the most unstable mode in MEGA is computed in the presence of background perturbations, while the CGM linear stability is computed with both AE mode and background turbulence, it would be of interest to compare the critical gradients for these two models. For MEGA, the critical gradient is defined as the value when the mode can no longer be excited in the nonlinear phase. The analysis is presented in Appendixes A and B, which shows that the error between two critical gradients is 5% and the error increase to 17% by considering multiple AEs. Furthermore,
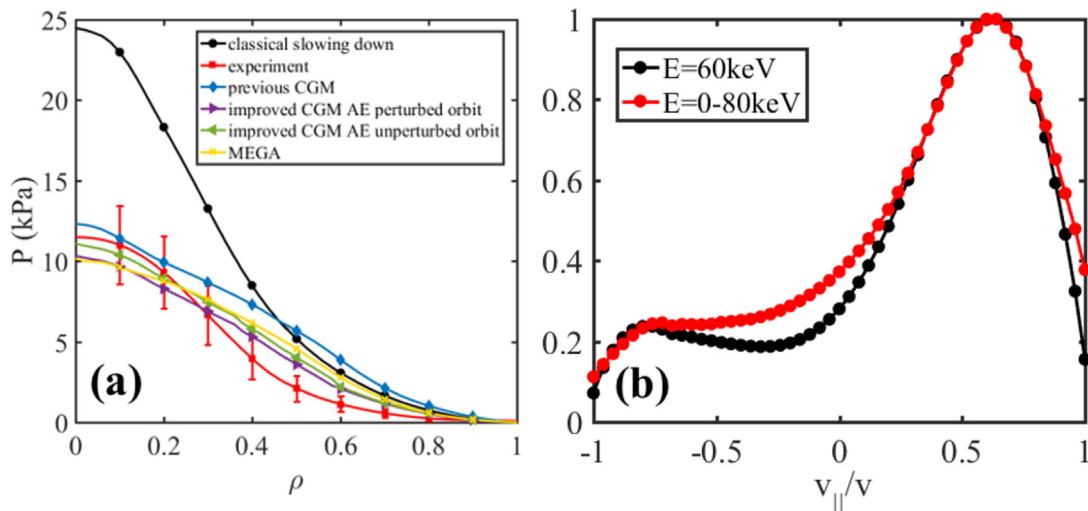

FIG. 10. (a) Density profile comparison: black curve represents classical slowing down, the red curve is inferred from experiment data, blue curve represents original CGM without loss cone effect, purple/green curve is improved CGM with loss cone from AE perturbed/unperturbed orbits, (b) EP redistribution in pitch angle space. The random error in the experimental fast-ion pressure associated with subtraction of the thermal pressure is indicated by the error bar in (a).

the gap between that and the single mode linear stability threshold is of the order of the gradient needed to sustain EP transport by background turbulence.

As a separate check, the normalized pitch-angle distribution from the improved CGM simulation is depicted in Fig. 10(b), where the black curve represents the distribution with $E = 60\,keV$ and the red curve contains all energy. The peak disappears in the negative pitch angle, which is consistent with the placement of the loss cone. This feature is also similarly exhibited in the MEGA multi-phase simulation.[55]

B. Discharge #153071

In discharge #153071, TAEs are destabilized at larger minor radius with $f = 100–200\,kHz$,[53] but the modes have a wide structure with $\rho = 0.2–0.6$ by neglecting toroidal rotation. Resembling Sec. IV A, we focus on the $n = 4$ TAE (Fig. 11), which has the largest linear growth rate. Cosine and sine parts of the radial velocity of an $n = 4$ TAE are depicted by solid and dashed curve, respectively. Loss cones due to FOW effects are depicted in Fig. 12. Because of weak amplitude and small radial overlap between AE unstable region and loss cone, AE perturbations are not included in the loss cone calculation.

Similar to Sec. IV A, using the defined threshold and loss cone, the EP redistribution is calculated by the improved CGM. To compare with experiment data (green triangle), we display the simulated pressure profile (red curve) in Fig. 13. The redistribution profile resembles a Gaussian function and shows good agreement within the measured pressure profile error bars with minor exceptions. For comparison, the pressure calculated by classical slowing down and previous CGM are depicted by the black and blue curves. The improved agreement with the modified CGM is clear, as is the effect of adding the loss cone in the middle part of the minor radii.
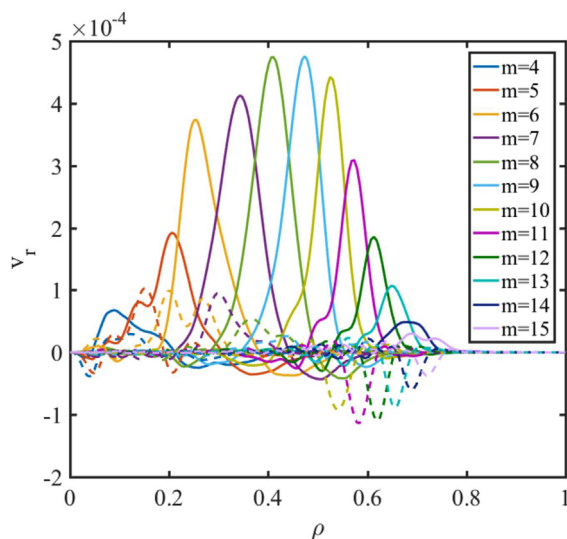

FIG. 12. Loss boundary in $(\rho, v_{||}/v)$ space with different energies. ORBIT results are depicted by points, which are connected by the corresponding solid curves. The loss region is on the right side of the curve.

V. EP REDISTRIBUTION FOR CFETR STEADY STATE SCENARIO

Encouraged by the benchmarking results of the improved CGM with experiments, it is of interest to use the same method to predict alpha particle redistribution for CFETR steady state scenario. The equilibrium is obtained by integrated simulation through the OMFIT framework.[57] Although the integrated simulation includes both alpha particle and neutral beam, we only consider alpha particle in this paper. Previous observations of TFTR[58,59] indicated NBI could mitigate the AE driven by the alpha particles. This effect is not considered in our study and could lead to an over-estimation of the EP redistribution. For the CFETR scenario in consideration, on-axis magnetic field

FIG. 11. Spatial profile of $n = 4$ TAE with $m = 4–15$ calculated by MEGA. Cosine and sine part of radial velocity are depicted by solid and dashed curve, respectively.

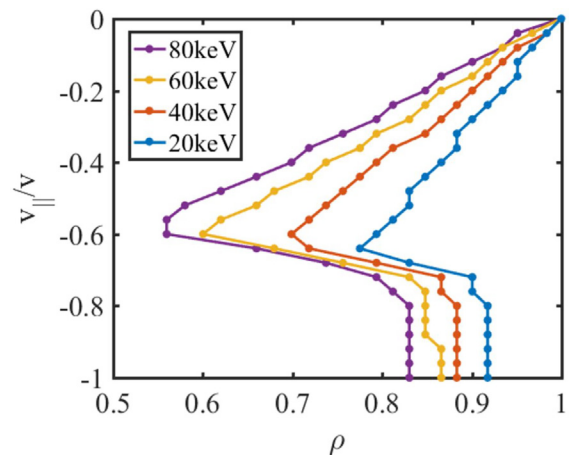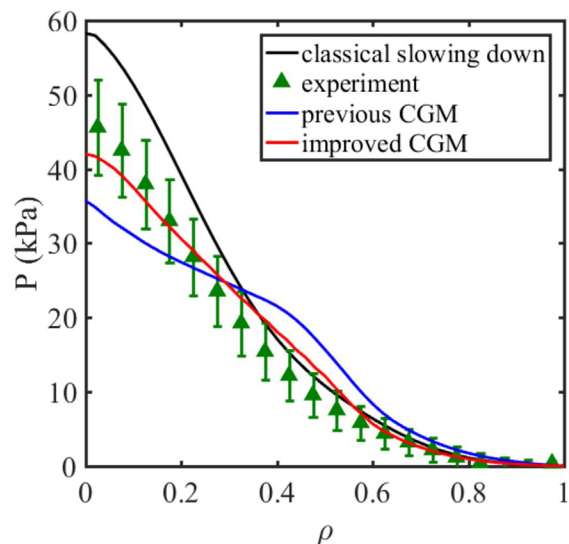FIG. 13. Pressure profile of classical slowing down (black), previous (blue) and improved (red) CGM. For comparison, experimental data[39] are depicted by green triangles with error bar.
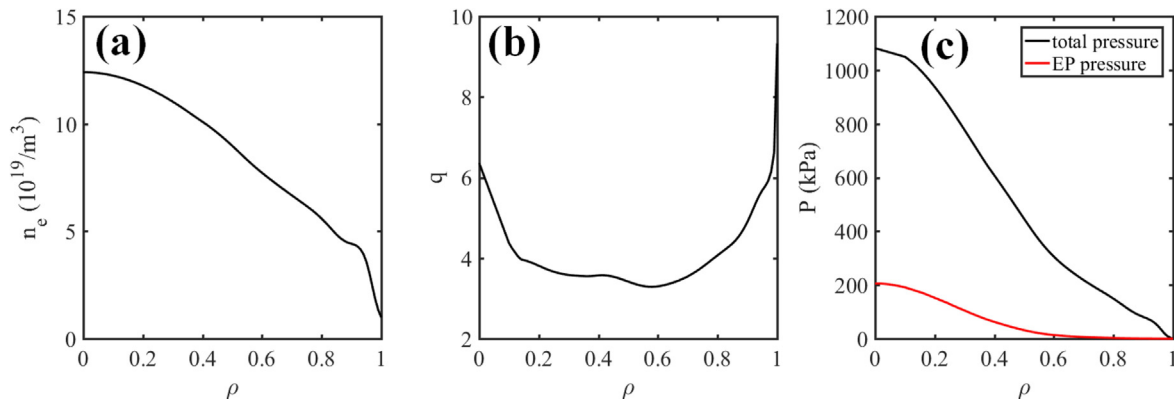
FIG. 14. Plasma profile of CFETR steady state scenario (a) electron density (b) safety factor (c) pressure, where total pressure is depicted by the black curve and EP pressure is depicted by red curve.

$B = 6.5$ T and plasma current $I = 12$ MA. The geometry parameters are $R = 7.2$ m, $a = 2.2$ m, $\kappa = 2.0$, and $\delta = 0.5$. Figure 14 panel (a) shows the electron density profile, panel (b) shows the safety factor profile and panel (c) shows the pressure profile, where the black curve is the total pressure and the red curve is the classical slowing-down alpha pressure using Eq. (7) with DT background only. In classical slowing down model, the alpha particles are generated by fusion reactions with the isotropic source, so that the alpha profile corresponds to the background D-T profile. However, neoclassical transport theory and an anisotropic birth profile would make α-particle distribution anisotropic,[60] which is ignored in this paper.

The NOVA code[61] is employed to calculate $n = 1$–10 TAEs and RSAEs. Due to the large size of the device, $n = 6$–10 TAEs are dominant with $n = 6$ having the largest growth rate in the core. AEs are allowed in a wide radial range because of the quite flat q profile. Figure 15(a) depicts the $n = 3, 5, 7$ TAEs (note the mode with the lowest frequency for $n = 3$ is an RSAE) in the continuum, where toroidal mode number is distinguished by different colors. Considering plasma toroidal rotation, the TAE gap has a Doppler shift ($\Delta f = n f_{rot}$) for each n.[62] AEs exist near the location of q_{min} within a wide range of $\rho = 0.4$–0.8 because of the flat q profile. Each horizontal line represents a solution for AE, but not all of these solutions could be excited. Instead of finding a

single dominant toroidal mode as in Sec. IV, there could be several dominant n modes in the unstable region of CFETR. For this reason, $n = 1$–10 are considered in TGLFEP. The growth rate (γ/ω) of TAEs calculated by TGLFEP are depicted in Fig. 15(b), which indicates AEs are most unstable in the core ($0.3 < \rho < 0.5$) and stable with $\rho > 0.7$. The most unstable mode is selected to calculate a local threshold in each flux surface. Consistent with TGLFEP, NOVA indicates the AEs in the core are more unstable. Figure 15(c) depicts the most unstable TAE with $n = 5$. The ORBIT results (Fig. 16) indicate that the EP loss cone is quite small due to the high magnetic field, and the deepest penetration of the loss boundary of 3.5 MeV particles is at $\rho = 0.67$, where AE growth rates are still quite low. Thus, AEs are not included in the ORBIT loss cone calculation. As we discussed in Sec. III B, dashed curves of Fig. 16(a) represent the loss cone by setting initial EPs at the inside midplane. The loss boundary of 3.5 MeV particles peaks at $\rho = 0.83$, which is larger than the case with initial EPs at the outside midplane. Since the grid is set sparsely in energy space, the boundaries of different energies appear overlapped. For example, in Fig. 16(b) the trajectory with initial EP at the outside (inside) midplane is depicted by a blue (red) curve. The arrow shows the direction and the cross marks the lost position of the LCFS.
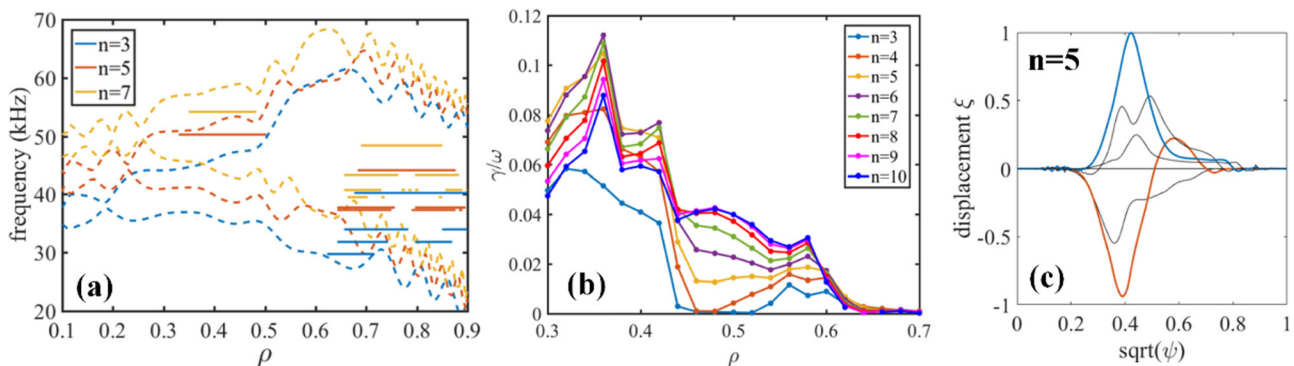

FIG. 15. (a) $n = 3, 5, 7$ continuum and AEs location calculated by NOVA. The mode with the lowest frequency for $n = 3$ is an RSAE. The frequency of TAE gap has a Doppler shift by considering plasma rotation. (b) The growth rate of TAEs with $n = 3$–10 as a function of minor radius calculated by TGLFEP. (c) Mode structure with $n = 5$.
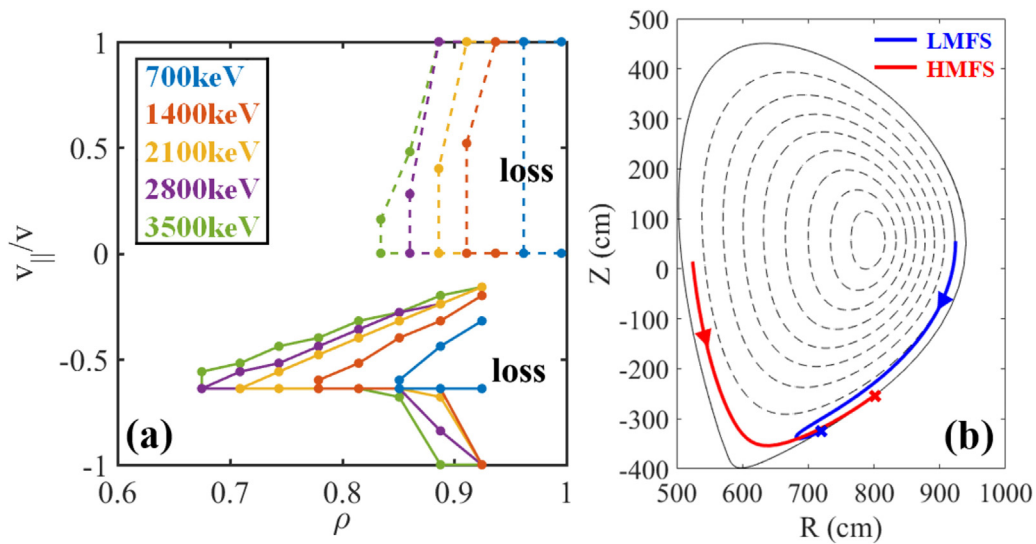
FIG. 16. (a) Loss boundary in pitch angle space as a function of poloidal flux ψ with different energies distinguished by colors. The solid curves depict initial EPs at the outside midplane, and dashed curves depict initial EPs at the inside midplane. (b) Trajectories of lost particles with initial EPs at the outside midplane (blue) and inside midplane (red).

Following Secs. II–IV, we discuss three EP transport/loss mechanisms in the improved CGM: turbulent transport by the Angioni model, radial transport induced by unstable AEs, and losses due to FOW effect. With the three mechanisms turned on, the predicted EP redistribution is identified by the red curve in Fig. 17(a). Other predictions obtained by isolating selected mechanisms are added for comparison. The black curve shows the classical slowing down distribution from Eq. (7) (before transport), and the blue curve shows the redistribution by turbulence and AE (without FOW). Additionally, in Fig. 17(b), the yellow curve represents the redistribution by only FOW, the green curve represents the redistribution by only turbulence, and the pink dashed curve represents the redistribution by the combination of

turbulence and FOW (without AE). The specific loss fraction (compared with classical slowing down) of each curve is listed in Table I. From the comparison, it can be concluded that (1) Large magnetic field and current reduce the EP loss cone, which is favorable for EP confinement, so that FOW loss is only ∼1%. (2) Turbulent transport leads to only small EP radial transport, and negligible EP loss across the LCFS ∼0.7%. However, unstable AEs raise the local diffusion coefficient, which enhance EP loss across the LCFS ∼5.9%. (3) EP radial transport pushes particles into the loss cone region to enhance EP orbit loss. The combination of background turbulent transport and FOW increases the loss to ∼2.5%, which is larger than the linear superposition of the two mechanisms. (4) Approximately 9.6% EP loss
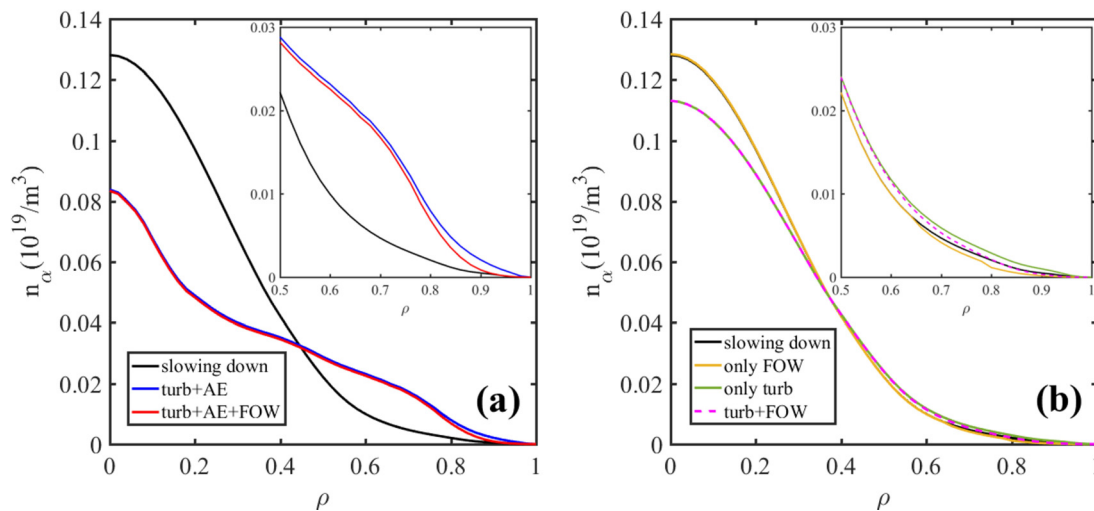

FIG. 17. Comparison of EP redistribution density profile. (a) black: classical slowing down, blue: turbulence and AE, red: combination of turbulence, AE and FOW (b) green: only turbulence, yellow: only FOW, pink dash: combination of turbulence and FOW. The profiles with $\rho > 0.5$ are enlarged in the insets.

TABLE I. Comparison of EP density and loss fraction with the inclusion of various transport mechanisms in a CFETR steady state scenario plasma.

Curve	Density on axis $(10^{19}\,\mathrm{m}^{-3})$	Loss fraction (%)
Classical slowing down	0.128	/
Only turbulence	0.113	0.7
Only FOW	0.128	1.0
Turbulence + AE	0.084	5.9
Turbulence + FOW	0.113	2.5
Turbulence + AE + FOW	0.083	9.6

is estimated by the improved CGM, which is dominated by the AE transport modification of the slowing down profile. It pushes more EPs to the outer region and into the loss cone. As a result, the radial profile for alpha particle heating estimated using a classical slowing-down distribution becomes inaccurate, which could quantitatively affect the fusion performance prediction for CFETR scenarios. Encouragingly, the ~9.6% loss for the CFETR scenario is far less than the ~50% loss in the DIII-D shot #142111. We attribute this to the clear separation between the AE unstable region [$0.3 < \rho < 0.5$ in Fig. 11(a)] and the loss cone region [$\rho > 0.7$ in Fig. 17(a)].

VI. CONCLUSION

In this paper, we have introduced a simulation method provided by Waltz *et al.* based on the theory of critical gradient model (CGM). The method aims to fast predict EP redistribution in the presence of unstable AEs by the combination of two codes, TGLFEP and EPtran. However, due to an assumption to expedite the code as well as some missing physics in the original model, the predicted EP density profile is abnormally flat in the AE unstable region and the number of EPs near the edge is over-predicted when compared with DIII-D experiment. This motivated two improvements to the CGM to enhance the accuracy of the EP redistribution profile prediction. First, we use the normalized critical L_{nEP} to replace the density gradient as the physical quantity for marginal stability assessment and revise the corresponding formula for diffusion coefficient motivated by established linear stability theory. The threshold scanning method of the TGLFEP is modified. Supported by the scanning result, the critical L_{nEP} is defined as an inversely proportional function of EP density, and the coefficients are calculated in each surface by TGLFEP, so that the threshold could evolve straightforwardly during EP transport. Second, the ORBIT code is used to calculated the EP loss cone in phase space, which is incorporated into the EPtran code to estimate additional EP losses inside the LCFS due to FOW effect.

The improved simulation method is benchmarked with DIII-D discharges #142111 and #153071 using the most unstable toroidal mode at each flux surface across the minor radius. The TAE mode structure is calculated by MEGA, and the linear growth rate and critical density calculated by TGLFEP. The ORBIT code calculates the loss cone by setting initial EPs at the outside midplane. Importantly, the modification of the loss cone by unstable AE is included. Using this combination, the EP redistribution calculated by EPtran demonstrates a much better agreement with experimental results across the entire minor radius, and the profile is consistent with MEGA result in

pitch-angle space. The predicted fractional EP loss of 42% is also similar to experimental observation.

The AE-induced EP transport in CGM and MEGA is based on very different physics although they both share the characteristic of a critical gradient, which yields a redistributed EP profile. A comparison between TGLFEP and MEGA on the saturated EP profiles and the critical threshold gradients leads to two observations. The critical threshold for MEGA could be approximated by the EP density gradient when the most unstable mode(s) in the presence of background perturbations could no longer grow in the nonlinear phase. Furthermore, the gap between that and the single mode linear stability threshold in CGM is of the order of the gradient needed to sustain EP transport by background turbulence. Extensive comparisons will be needed to draw firm conclusions on these two observations. Some deficiencies of CGM are also highlighted, which include the ability to treat multiple unstable modes at the same location, and accounting for modes destabilized by nonlocal mode-mode coupling. These will be left as future improvements for CGM.

An advantage of CGM is its computational efficiency for reactor design. As an application, α particle redistribution is predicted by the same method for CFETR steady state scenario. Multiple unstable TAEs (RSAE for part of the toroidal mode spectrum) are found over a wide range of minor radii due to the flat q profile, and n = 7–10 AEs are dominant. The critical gradient profile is quite flat in the AE unstable region. Fortunately, the high magnetic field (6.5 T) and current shrinks the loss cone effectively, which is favorable for EP confinement. Three EP transport mechanisms (turbulent transport by the Angioni model, radial transport induced by unstable AE, and losses due to FOW effect) and their coupling effects are discussed. The comparison of EP redistribution profile indicates that turbulent transport only causes slight EP distribution modification. In spite of the enhanced radial transport, only a small EP loss ~3.8% is induced by AE across the LCFS. The FOW effect provides a sink of EP particles at larger minor radii, which acts in concert with AE diffusion in the core. Each of the three mechanisms by itself only results in a slight EP loss, but the combination of AE enhanced transport and FOW raises the loss up to ~9.6%, which is still significantly smaller than that observed in present experiments. Since the loss cone is determined by the equilibrium and AE instability is sensitive to the q profile, the coupling effect of EP radial transport and FOW could be reduced effectively if (i) the loss cone and the unstable AE region is well-separated, and (ii) the width of the unstable AE is sufficiently narrow to minimize strong diffusion. Optimization of CFETR scenario to reach this goal will be our next step.

AUTHOR DECLARATIONS

Conflict of Interest

I declare there is no conflict of interest.

DATA AVAILABILITY

The data that support the findings of this study are available within the article.

APPENDIX A: THE RECIPE FOR MARGINAL STABILITY

In previous simulations, the method of the critical gradient calculation was to scan the EP density (density gradient) with fixed characteristic length of EP density ($L_{n_{EP}} = -n_{EP}/(\partial n_{EP}/\partial r)$) until AEs were found to be marginally stable. Obviously, the key point

was to determine the recipe for marginal stability, which was set as (i) $\gamma_{AE} = \gamma_{ITG/TEM}$, (ii) $\gamma_{AE+ITG/TEM} = \gamma_{ITG/TEM}$, (iii) $\gamma_{AE} = 0$, and (iv) $\gamma_{AE+ITG/TEM} = \gamma_{ITG/TEM} + \alpha\gamma_E/|\hat{s}|$, respectively.[24,51] In Ref. 51, recipe (ii) was verified to be closer to the nonlinear simulation than recipe (i), and Fig. 2 of Ref. 51 indicated the thresholds calculated by recipe (ii) and recipe (iii) were consistent. The recipe (iv) includes the effect of equilibrium $E \times B$ velocity shear, but the coefficient α needed to be fitted by the experiment, besides the recipe (iv) cannot be used for shear-reversal surface. Thus, we select recipe (ii) for this paper, recognizing the estimated threshold will be lower than recipe (iv) for DIII-D. For cases with low toroidal rotation, such as CFETR, the effect can be neglected.

In Ref. 24, the recipe was studied through local and global simulation by GYRO, which revealed that the strongest local growth rate was larger than the global growth rate, while the corresponding threshold was lower than that from the global simulation. For our study, the threshold between two codes with different theoretical bases is compared. We use TGLFEP for the local simulation, since the consistency between TGLF and GYRO is well established.[30] Our global simulation employs MEGA, since MEGA uses an MHD-gyrokinetic model, which is different from the gyrokinetic GYRO and the gyro-Landau-fluid TGLF. However, both approaches allow coupling to the background. The comparison between the two codes for the n = 3 TAE of discharge #142111, which is the most unstable mode, is displayed in Fig. 18. Since the peak of n = 3 TAE calculated by MEGA is at $\rho = 0.4$, where TGLFEP obtains the largest linear growth rate, we select this position to compare the two codes. In Fig. 18(a), TGLFEP results are depicted by a red curve for AE growth rate, and a green curve for the background turbulent growth rate, so the intersection (vertical red dashed line) represents the defined normalized critical density ($n_{EP}/n_{SD} = 0.38$), where n_{EP} means energetic particle density and n_{SD} means the original
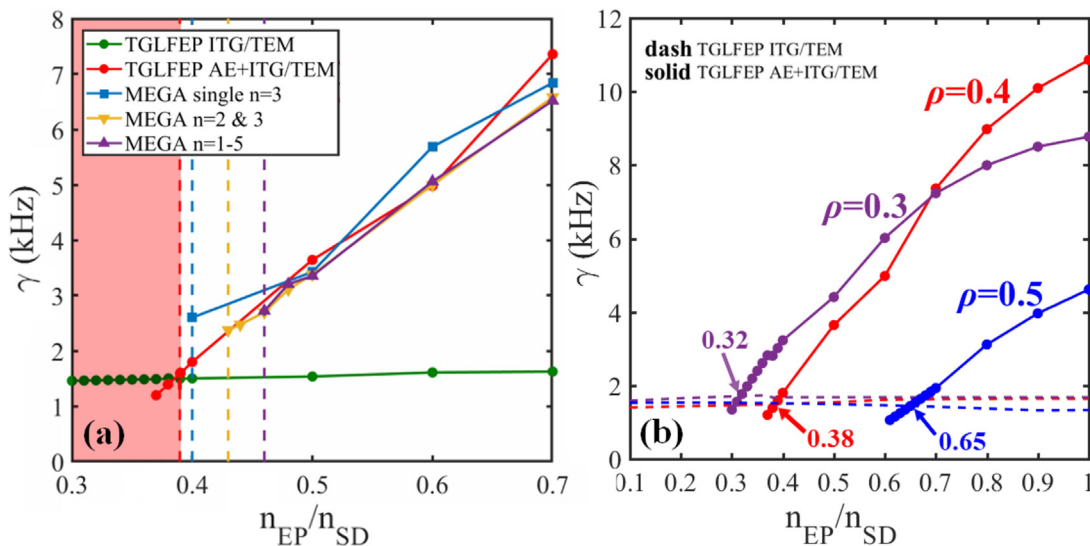
FIG. 18. (a) Comparison between TGLFEP and MEGA on the critical density (gradient) scanning. By using the recipe of $\gamma_{AE+ITG/TEM} = \gamma_{ITG/TEM}$ for marginal stability, the cross of the red and green curve means the threshold obtained by TGLFEP. Blue, orange, and purple curves represent single n = 3, n = 2–3, and n = 1–5 simulations by MEGA, respectively. The vertical dashed line marks threshold with corresponding color. (b) Threshold calculation by TGLFEP for different locations.

FIG. 19. Mode structures of $n = 3$ with decreasing n_{EP}/n_{SD} after $\sim 800\ t_A$ for MEGA $n = 1$–5. (a) $n_{EP}/n_{SD} = 0.5$, (b) $n_{EP}/n_{SD} = 0.46$, (c) $n_{EP}/n_{SD} = 0.44$.
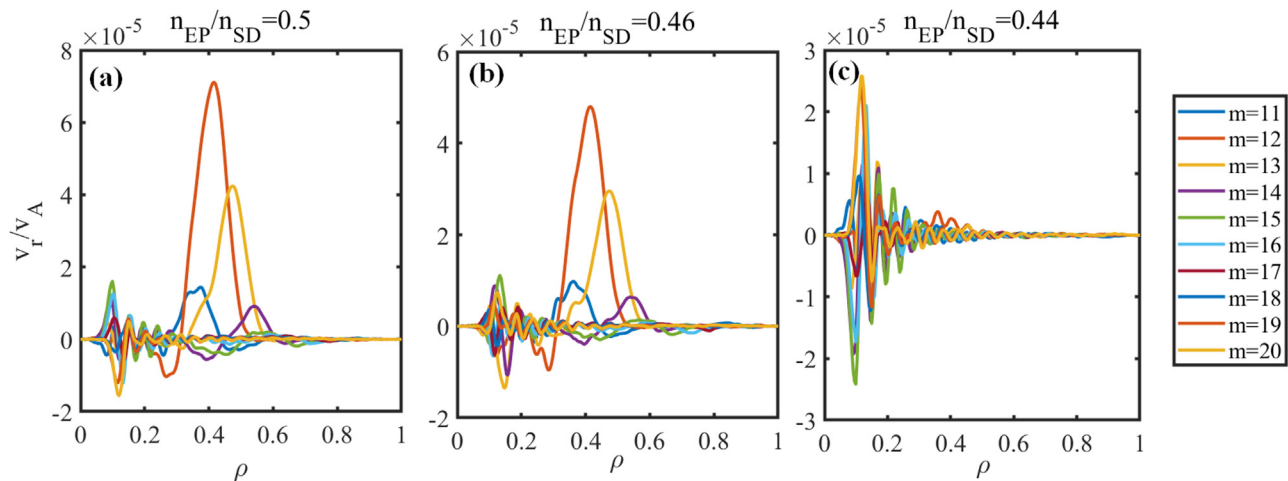
energetic particle slowing-down density. In MEGA scanning, the whole EP pressure profile moves down with a fixed characteristic length of EP as constrained by MEGA until the AE is not dominant, i.e., the displacements of $m = 12$ and $m = 13$ harmonics, which represent the dominant components of a TAE, become intermingled with background perturbations for $n = 3$ case. Each simulation is carried out up to and beyond 1000 Alfvén times (significantly beyond the linear phase) to ensure that either a distinct $n = 3$ mode or an intermingled background is robust. The blue curve represents the linear growth rate of $n = 3$ TAE with single n simulation, and the purple curve for multiple n ($n = 1$–5) simulation, with critical $n_{EP}/n_{SD} = 0.4$ and 0.46, respectively. Corresponding to the purple curve, the mode structures of $n = 3$ with the decreasing n_{EP}/n_{SD} are exhibited in Fig. 19. We can observe a typical TAE structure only with $n_{EP}/n_{SD} \geq 0.46$, which is defined to be the threshold. At $n_{EP}/n_{SD} = 0.44$, we clearly see a strong coupling to background perturbation. The perturbation represents MHD modes since it persists over many Alfvén times. MEGA is a non-perturbative global MHD code. During nonlinear evolution, unstable AE changes the total pressure profile, which could drive other MHD modes unstable. This secondary induced instability could be considered as a damping mechanism that prevents AE growth when it is close to the marginal stability.

The MEGA single n simulation threshold compares quite well ($<5\%$) with the TGLFEP threshold. If multiple unstable n modes are used in the global code, the predicted threshold is somewhat larger ($<17\%$). This can be explained by energy being channeled from the main mode to the other modes, which increases the effective damping rate. In Fig. 18(a), we also plotted the MEGA growth rate and critical threshold with only the two most unstable modes, i.e., $n = 3$ and 2. As expected, the critical threshold is much closer to that for a single $n = 3$ simulation. Furthermore, the linear stability threshold for TGLFEP can be obtained from Fig. 18(a) by extending the red curve all the way to $\gamma = 0$ yielding $n_{EP}/n_{SD} = 0.30$. The difference between that and the MEGA nonlinear stability threshold is of the order of the additional gradient needed

to balance the EP transport caused by background turbulence in CGM.

MEGA calculates a fixed threshold across the entire mode width. This linear estimate is too crude to model the change in EP profile since we know from experiment that the EP profile changes in a finer scale than the AE mode width. For this reason, a local stability code TGLFEP is used to calculate the local critical threshold. At each location, TGLFEP is first used to compute the most unstable n mode (we did not *a priori* fix the n value across the entire radii). It turned out $n = 3$ is dominant across the mode width predicted by MEGA for discharge #142111, which is another consistency check of TGLFEP. Figures 18(b) and 20 show, indeed, that the local critical threshold exhibits some variation as needed to model the finer scale of the EP profile variation.
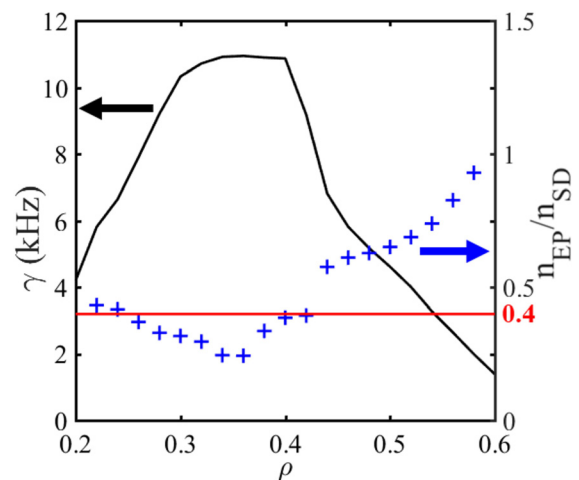

FIG. 20. Linear growth rate (black curve) and critical density (blue cross) vs minor radius. The red horizontal line represents the threshold obtained by MEGA.

APPENDIX B: TURBULENT DIFFUSIVITY OF ANGIONI MODEL

For AE stable location, we can obtain a simple expression of flux from Eqs. (2) and (3) by ignoring Γ^E and $\partial f/\partial E$,

$$\Gamma^r(r, E) = -D_{ITG/TEM} \frac{\partial f_{EP}}{\partial r}. \tag{B1}$$

For the energy-independent model

$$D_{ITG/TEM} = D_{He}\left[0.02 + 4.5(T_e/E_\alpha) + 8(T_e/E_\alpha)^2 + 350(T_e/E_\alpha)^3\right], \tag{B2}$$

where D_{He} is Helium diffusivity set to the effective thermal plasma diffusivity $D_{He} \approx \chi_{eff} = \chi_i + \chi_e$, T_e is electron temperature, and E_α is initial EP energy (injected energy for NBI/birth energy for α particle). Thus, the $D_{ITG/TEM}$ is independent with EP energy.

For the energy-dependent model

$$D_{ITG/TEM} = \frac{G_D}{\langle G_D \rangle_s} D_{He}[0.02 + 4.5(T_e/E_\alpha) \\ + 8(T_e/E_\alpha)^2 + 350(T_e/E_\alpha)^3], \tag{B3}$$

where

$$G_D(E/T_e) = 1.25 \text{ for } E/T_e \leq 2.7,$$
$$G_D(E/T_e) = \exp\left[-8.14 \times 10^{-5}(E/T_e)^4 + 3.77 \times 10^{-3}(E/T_e)^3 \\ -0.0553(E/T_e)^2 + 0.036(E/T_e) + 0.45\right]$$
$$\text{for } E/T_e > 2.7, \tag{B4}$$

$$\langle[\cdots]\rangle_s = \frac{\int f_s[\cdots]\left(2\pi\sqrt{E}\right)dE}{\int f_s\left(2\pi\sqrt{E}\right)dE}. \tag{B5}$$

So that $D_{ITG/TEM}$ is dependent with EP energy. If we ignore the effect of energy, Eq. (B3) will return to Eq. (B2). The details can be found in Refs. 28 and 33.

REFERENCES

[1] Y. Wan, J. Li, Y. Liu, X. Wang, V. Chan, C. Chen, X. Duan, P. Fu, X. Gao, K. Feng et al., Nucl. Fusion **57**(10), 102009 (2017).

[2] G. Zhuang, G. Q. Li, J. Li, Y. X. Wan, Y. Liu, X. L. Wang, Y. T. Song, V. Chan, Q. W. Yang, B. N. Wan et al., Nucl. Fusion **59**(11), 112010 (2019).

[3] J. D. Gaffey, Jr., J. Plasma Phys. **16**(2), 149–169 (1976).

[4] C. Estrada-Mila, J. Candy, and R. E. Waltz, Phys. Plasmas **13**, 112303 (2006).

[5] M. A. Van Zeeland, W. W. Heidbrink, R. K. Fisher, M. García Muñoz, G. J. Kramer, D. C. Pace, R. B. White, S. Aekaeslompolo, M. E. Austin, J. E. Boom et al., Phys. Plasmas **18**, 056114 (2011).

[6] W. W. Heidbrink, C. S. Collins, M. Podestà, G. J. Kramer, D. C. Pace, C. C. Petty, L. Stagner, M. A. Van Zeeland, R. B. White, and Y. B. Zhu, Phys. Plasmas **24**, 056109 (2017).

[7] M. Garcia-Munoz, I. G. J. Classen, B. Geiger, W. W. Heidbrink, M. A. Van Zeeland, S. Äkäslompolo, R. Bilato, V. Bobkov, M. Brambilla, G. D. Conway et al., Nucl. Fusion **51**, 103013 (2011).

[8] V. G. Kiptily, C. P. Perez von Thun, S. D. Pinches, S. E. Sharapov, D. Borba, F. E. Cecil, D. Darrow, V. Goloborod'ko, T. Craciunescu, T. Johnson et al., Nucl. Fusion **49**, 065030 (2009).

[9] M. Ishikawa, M. Takechi, K. Shinohara, C. Z. Cheng, G. Matsunaga, Y. Kusama, A. Fukuyama, T. Nishitani, A. Morioka, M. Sasao et al., Nucl. Fusion **47**, 849 (2007).

[10] E. D. Fredrickson, C. Z. Cheng, D. Darrow, G. Fu, N. N. Gorelenkov, G. Kramer, S. S. Medley, J. Menard, L. Roquemore, D. Stutman et al., Phys. Plasmas **10**, 2852 (2003).

[11] W. Zhang, Z. Lin, and L. Chen, Phys. Rev. Lett. **101**, 095001 (2008).

[12] K. Ghantous, N. N. Gorelenkov, H. L. Berk, W. W. Heidbrink, and M. A. Van Zeeland, Phys. Plasmas **19**, 092511 (2012).

[13] E. M. Bass and R. E. Waltz, Phys. Plasmas **20**, 012508 (2013).

[14] R. B. White, N. Gorelenkov, W. W. Heidbrink, and M. A. Van Zeeland, Phys. Plasmas **17**, 056107 (2010).

[15] D. C. Pace, W. W. Heidbrink, and M. A. Van Zeeland, Phys. Today **68**(10), 34 (2015).

[16] C. S. Collins, W. W. Heidbrink, M. E. Austin, G. J. Kramer, D. C. Pace, C. C. Petty, L. Stagner, M. A. Van Zeeland, R. B. White, Y. B. Zhu et al., Phys. Rev. Lett. **116**, 095001 (2016).

[17] Y. Todo, M. A. Van Zeeland, A. Bierwage, W. W. Heidbrink, and M. E. Austin, Nucl. Fusion **55**, 073020 (2015).

[18] R. B. White and M. S. Chance, Phys. Fluids **27**, 2455 (1984).

[19] Y. Todo, K. Shinohara, M. Takechi, and M. Ishikawa, Phys. Plasmas **12**, 012503 (2005).

[20] Y. Todo, Phys. Plasmas **13**, 082503 (2006).

[21] M. Podestà, M. Gorelenkova, N. N. Gorelenkov, and R. B. Whit, Plasma Phys. Controlled Fusion **59**, 095008 (2017).

[22] M. Podestà, L. Bardóczi, C. S. Collins, N. N. Gorelenkov, W. W. Heidbrink, V. N. Duarte, G. J. Kramer, E. D. Fredrickson, M. Gorelenkova, and D. Kim, Nucl. Fusion **59**, 106013 (2019).

[23] E. M. Bass and R. E. Waltz, Phys. Plasmas **17**, 112319 (2010).

[24] R. E. Waltz, E. M. Bass, W. W. Heidbrink, and M. A. VanZeeland, Nucl. Fusion **55**, 123012 (2015).

[25] C. S. Collins, W. W. Heidbrink, M. Podestà, R. B. White, G. J. Kramer, D. C. Pace, C. C. Petty, L. Stagner, M. A. Van Zeeland, Y. B. Zhu et al., Nucl. Fusion **57**, 086005 (2017).

[26] J. Candy and R. E. Waltz, J. Comput. Phys. **186**(2), 545–581 (2003).

[27] R. E. Waltz and E. M. Bass, Nucl. Fusion **54**, 104006 (2014).

[28] C. Angioni and A. G. Peeters, Phys. Plasmas **15**, 052307 (2008).

[29] C. Angioni, A. G. Peeters, G. V. Pereverzev, A. Bottino, J. Candy, R. Dux, E. Fable, T. Hein, and R. E. Waltz, Nucl. Fusion **49**, 055013 (2009).

[30] S. He, R. E. Waltz, and G. M. Staebler, Phys. Plasmas **24**, 072305 (2017).

[31] G. M. Staebler, J. E. Kinsey, and R. E. Waltz, Phys. Plasmas **12**, 102508 (2005).

[32] E. M. Bass and R. E. Waltz, Nucl. Fusion **60**, 016032 (2020).

[33] H. Sheng and R. E. Waltz, Nucl. Fusion **56**, 056004 (2016).

[34] N. N. Gorelenkov, W. W. Heidbrink, G. J. Kramer, J. B. Lestz, M. Podesta, M. A. Van Zeeland, and R. B. White, Nucl. Fusion **56**, 112015 (2016).

[35] N. N. Gorelenkov, H. L. Berk, and R. V. Budny, Nucl. Fusion **45**, 226 (2005).

[36] N. N. Gorelenkov, C. Z. Cheng, and G. Y. Fu, Phys. Plasmas **6**, 2802 (1999).

[37] S. Taimourzadeh, E. M. Bass, Y. Chen, C. Collins, N. N. Gorelenkov, A. Könies, Z. X. Lu, D. A. Spong, Y. Todo, M. E. Austin et al., Nucl. Fusion **59**, 066006 (2019).

[38] M. A. Van Zeeland, N. N. Gorelenkov, W. W. Heidbrink, G. J. Kramer, D. A. Spong, M. E. Austin, R. K. Fisher, M. García Muñoz, M. Gorelenkova, N. Luhmann et al., Nucl. Fusion **52**, 094023 (2012).

[39] W. W. Heidbrink, J. R. Ferron, C. T. Holcomb, M. A. Van Zeeland, X. Chen, C. M. Collins, A. Garofalo, X. Gong, B. A. Grierson, M. Podestà et al., Plasma Phys. Controlled Fusion **56**, 095030 (2014).

[40] M. Podestà, M. Gorelenkova, and R. B. White, Plasma Phys. Controlled Fusion **56**, 055003 (2014).

[41] Y. Todo, H. L. Berk, and B. N. Breizman, Nucl. Fusion **50**, 084016 (2010).

[42] A. M. Dimits and W. W. Lee, J. Comput. Phys. **107**, 309 (1993).

[43] A. Y. Aydemir, Phys. Plasmas **1**, 822 (1994).

[44] W. M. Tang, J. W. Connor, and R. J. Hastie, Nucl. Fusion **20**, 1439 (1980).

[45] L. Chen and C. Z. Cheng, Phys. Fluids **23**(11), 2242–2249 (1980).

[46] J. Lang, G. Y. Fu, and Y. Chen, Phys. Plasmas **17**, 042309 (2010).

[47] R. E. Waltz, E. M. Bass, and G. M. Staebler, Phys. Plasmas **20**, 042510 (2013).

[48] Z. Qiu, L. Chen, and F. Zonca, Nucl. Fusion **59**, 066024 (2019).

[49] R. Betti and J. P. Freidberg, Phys. Fluids B **4**(6), 1465–1474 (1992).

[50] A. Pankin, D. Mccune, R. Andre, G. Bateman, and A. Kritz, Comput. Phys. Commun. **159**, 157 (2004).

[51] E. M. Bass and R. E. Waltz, Phys. Plasmas **24**, 122302 (2017).

[52] L. L. Lao, H. S. John, R. D. Stambaugh, A. G. Kellman, and W. Pfeiffer, Nucl. Fusion **25**(11), 1611 (1985).

[53] G. J. Kramer, M. Podestà, C. Holcomb, L. Cui, N. N. Gorelenkov, B. Grierson, W. W. Heidbrink, R. Nazikian, W. Solomon, M. A. Van Zeeland *et al.*, Nucl. Fusion **57**, 056024 (2017).

[54] C. T. Holcomb, W. W. Heidbrink, J. R. Ferron, M. A. Van Zeeland, A. M. Garofalo, W. M. Solomon, X. Gong, D. Mueller, B. Grierson, E. M. Bass *et al.*, Phys. Plasmas **22**, 055904 (2015).

[55] Y. Todo, M. A. Van Zeeland, A. Bierwage, and W. W. Heidbrink, Nucl. Fusion **54**, 104012 (2014).

[56] M. A. Van Zeeland, C. S. Collins, W. W. Heidbrink, M. E. Austin, X. D. Du, V. N. Duarte, A. Hyatt, G. Kramer, N. Gorelenkov, B. Grierson *et al.*, Nucl. Fusion **59**, 086028 (2019).

[57] O. Meneghini, S. P. Smith, L. L. Lao, O. Izacard, Q. Ren, J. M. Park, J. Candy, Z. Wang, C. J. Luna, V. A. Izzo *et al.*, Nucl. Fusion **55**(8), 083008 (2015).

[58] G. Y. Fu, C. Z. Cheng, R. Budny, Z. Chang, D. S. Darrow, E. Fredrickson, E. Mazzucato, R. Nazikian, and S. Zweben, Phys. Rev. Lett. **75**, 2336 (1995).

[59] G. Y. Fu, C. Z. Cheng, R. Budny, Z. Chang, D. S. Darrow, E. Fredrickson, E. Mazzucato, R. Nazikian, K. L. Wong, and S. Zweben, Phys. Plasmas **3**, 4036 (1996).

[60] V. Yavorskij, V. Goloborod'ko, L. G. Eriksson, V. Kiptily, K. Schoepf, and S. E. Sharapov, J. Fusion Energy **34**(4), 774–784 (2015).

[61] C. Z. Cheng, Phys. Reports **211**(1), 1–51 (1992).

[62] G. J. Kramer, R. Nazikian, B. Alper, M. de Baar, H. L. Berk, G.-Y. Fu, N. N. Gorelenkov, G. McKee, S. D. Pinches, and T. L. Rhodes, Phys. Plasmas **13**, 056104 (2006).